ACHIEVING LARGE STABLE VERTICAL DISPLACEMENT IN SURFACE-MICROMACHINED MICROELECTROMECHANICAL SYSTEMS (MEMS)

by

Erik R. Deutsch

B.A. Vassar College (May 1996)
M.S. Massachusetts Institute of Technology (June 1998)

Submitted to the Department Of Electrical Engineering and Computer Science
in Partial Fulfillment of the Requirements for the Degree of

Doctor of Philosophy

at the Massachusetts Institute of Technology

June 2002

Signature of Author .....
Department of Electrical Engineering and Computer Science
June 1, 2002

Certified by .....
Stephen D. Senturia, Barton L. Weller Professor
Department of Electrical Engineering and Computer Science
Thesis Supervisor

Certified by .....
Rajeev Ram, Associate Professor
Department of Electrical Engineering and Computer Science
Thesis Supervisor

Accepted by .....
Arthur C. Smith
Department of Electrical Engineering and Computer Science
Chairman, Department Committee on Graduate Students

Achieving Large Stable Vertical Displacement in Surface-Micromachined Microelectromechanical Systems (MEMS)

by

Erik R. Deutsch

Submitted to the Department Of Electrical Engineering and Computer Science
in Partial Fulfillment of the Requirements for the Degree of Doctor of Philosophy

ABSTRACT

This thesis describes electrostatic actuation techniques and mechanical design features for realizing large planar analog vertical travel in an electrostatically actuated diffractive mid-infrared optical device, which is robust, both to manufacture, and against pull-in during use. This device, called the *Polychromator*, is fabricated by polysilicon surface-micromachining and consists of many parallel elements, each 20 microns wide and a centimeter in length. Typically, achieving such a large travel would require prohibitively large gaps and actuation voltages. In order to reduce the actuation voltage and achieve greater travel before pull-in, thinner beams are used which exploit stress stiffening. This, in turn, creates a number of stress control hazards because tensile stress in one layer can induce buckling in a lower layer. These issues have been solved with detailed attention to supports and their compliance. A multi-layer nonlinear spring has been incorporated to make the device robust against pull-in. The electromechanical behavior of the device is simulated using Energy Methods, Finite Difference Methods, and the MEMCAD software. Excellent agreement between MEMCAD simulation and experimental measurements for this structure are reported. Each detail, stress control, support structure, and pull-in, must be addressed in order to achieve the combined effects of large travel, robustness against pull-in, and optically flat beams. Controlled planar actuation over a large vertical range at low applied voltages is obtained by combining a robust electromechanical design with a manufacturable surface micromachining process. Covering a centimeter square area, the 512 grating elements achieved 3.8 microns vertical displacement at 72 Volts with a 0.5 Volt standard deviation, indicating uniform performance across the device. The development of the device has led to innovations in position control, fabrication processes, device design, and device testing.

Thesis Supervisors:	Stephen D. Senturia Weller Professor of Electrical Engineering
	Rajeev Ram Associate Professor of Electrical Engineering and Computer Science
Thesis Reader:	Jeffrey H. Lang Professor of Electrical Engineering and Computer Science

Acknowledgments

I would like to take this opportunity to thank the many individuals who have contributed to my personal and academic growth over the past six years culminating in the completion of this thesis.

First, I would like to thank my research supervisor Professor Steve Senturia, who introduced me to and sparked my interest in MEMS. Steve has guided me through six years of graduate school and research, has driven me to excel, and has given me the opportunity to work in this field both technically and financially. I would also like to thank thesis supervisor Rajeev Ram and thesis reader Jeff Lang for reviewing the thesis and serving on my committee.

I would like to thank the past and present members of the Polychromator team at MIT, including, Steve Senturia, Jay Bardhan, Alicia Volpicelli, Raj Sood, Srikar Vengallatore, Elmer Hung, and Mike Hopgood, at Honeywell Laboratories, Ben Hocker, Dan Youngner, David Arch, Aravind Padmanabhan, Bill Herb, Dane Larson, and Steve Swanson, at Sandia National Laboratories, Mike Butler, Mike Sinclair, Ted Plowman, Hopper Chu, and at ACLARA BioSciences, Tony Ricco. Technical discussions with the members of the Polychromator team at Honeywell and Sandia have been insightful and helpful in many ways.

The members of my research group have been influential in making this work a success. I learned a great deal about MEMS and the Polychromator project from Elmer. My officemates, Jay, Raj, and Alicia made significant technical contributions, and provided much needed distractions. Jay Bardhan deserves special thanks for his help taking data for the Polychromator project, taking data with the automated testing system for this thesis, and for critically reviewing this thesis.

Several personal friends have been instrumental in my success, sanity, and enjoyment throughout the course of this thesis and the research leading to it. In particular I would like to thank Jay, Raj, Eric, John, Cynthia, Pei-Lin, Kamini, Kai, Yu-Han, Michelle, and Ritwik.

Finally, I would like to thank my parents John and Edna, my grandmother Maya, my sister Karin, and brother-in-law Indraneel, for their never ending love, support, and guidance throughout the path leading me to MIT and during my time here. Without them I would not be here today.

This work was sponsored, by DARPA under contract N6601-97-C-8620.

Table of Contents

Chapter 1: Introduction

Microelectromechanical systems (MEMS) are revolutionizing the field of optics. MEMS structures are suitably sized to interact well with light in reflective configurations such as the Texas Instruments Digital Micromirror Device [1] or in diffractive configurations such as the Silicon Light Machines Grating Light Valve [2]. When the reflective approach is implemented, the optical system external to the MEMS device determines the motion required by the device. When the diffractive approach is implemented, the motion required by the MEMS device is typically on the order of the incident wavelength. For visible light, this corresponds to approximately one half of one micron, which is readily achievable by surface micro-machined MEMS devices.

Specially designed phase or amplitude diffraction gratings have been shown (Sinclair et. al. [3,4]) to reproduce desired infrared spectra. A polychromatic spectrum is the result of diffraction from the optical elements in a grating (Figure 1.1). The grating described in this thesis is the Polychromator, an electronically programmable MEMS diffraction grating for use in a dark-field correlation spectrometer system. The previously reported Polychromator grating [5] has been designed to generate synthetic spectra in the 3 to 5 micron wavelength range. This grating will be referred to as the near-infrared Polychromator. The grating consists of 1024 individually addressable diffractive elements, 10 μm wide and 1 cm long. Diffractive elements must remain flat and their vertical positions must be controlled over an approximately 2 micron range for the device to correctly and efficiently generate synthetic spectra. This device has been fabricated and optimized for modest travel in previous work.

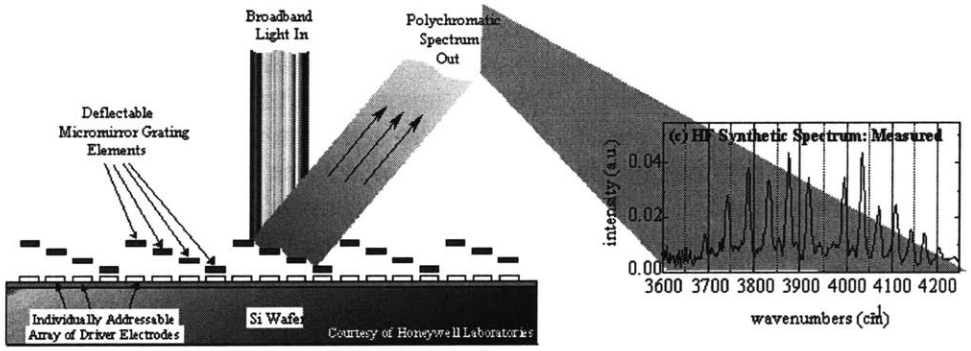

Figure 1.1: Polychromatic spectrum as a result of diffraction from MEMS grating.

The primary goal of this thesis is to design and fabricate a Polychromator device that extends the range of optical processing into the mid-infrared spectral region (Table 1.1). This spectral region is of particular interest because the characteristic absorption signatures of many chemicals lie within it. The challenge of this work is to push the limits of surface micromachining and electromechanical design, subject to two main constraints: low operating voltage and the requirement for large displacement. Specifically, the voltages are limited by the dielectric properties of the insulation layer used, and the displacement must be large enough to generate spectra in the 8 to 12 micron

wavelength range, which requires 4 to 6 microns of travel. Iterations between design and fabrication steps are essential to the successful production of a functional device.

Specification	Amount	Reason
Width of the elements	20 μm	Sets moderate diffraction angle Enables scalar diffraction theory
Vertical displacement	4 – 6 μm	Required by Fourier models
Number of grating elements	512	Provides adequate resolution
Length of the elements	1.2 cm	Results in a square die area

Table 1.1: Specifications for mid-infrared polychromator.

The manufacturing process must address significant challenges including the deposition and etching of thick oxide layers, stress control for structural polysilicon layers, dielectric insulation of conductors, metal adhesion, and the minimization of print-through topography. The electromechanical design is a multi-parameter, process dependent optimization to achieve pull-in protection, reduced support compliance, reduced end effects, low cross talk, minimal electrical leakage, low operating voltage, and large vertical displacement.

1.1 Large Travel Actuators

MEMS are used in a variety of fields, including optics, transportation, aerospace, robotics, chemical systems, biotechnology, and microscopy [6]. They are built using bulk or surface micromachining processes and are typically batch fabricated, similar to devices produced in the semiconductor industry. MEMS are typically used in these fields either as sensors, which convert mechanical actions to output signals, or as actuators, which convert input signals to mechanical actions. This section discusses actuators.

An actuator transfers energy from an input stimulus form into some type of displacement or mechanical response. Electrostatic actuation entails the application of a voltage difference to two conductors, which creates a force of attraction between the conductors and causes one or both of the conductors to move. Examples of this type of actuation are the Polychromator by Hocker et. al. [5], the DMD device by Van Kessel [7], an electrostatic microvalve by Sato et. al. [8], and adaptive optics devices by Tuantranont et. al. [9], and Bifano et. al. [10]. Thermal actuation exploits either a difference in the coefficient of thermal expansion (serpentine micro-bridges by Judy [11] or polyimide bimorph actuators by Ataka [12]), or a temperature difference (an optical microactuator by Huja [13]), to cause bending. Piezoelectric actuation is generated by the application of an electric field across a piezoelectric crystal, ceramic, or a thin film. The converse piezoelectric effect [14] then induces a strain, which translates into a displacement (a large displacement psuedo-static actuator by Toshiyoshi [15] or a two-dimensional micro scanner by Kawabata [16]). Magnetic actuation results from the force generated by a magnetic field; the fields are generally created by passing a current through a surface coil (the actuators described by Toshiyoshi [17], Liu [18], and Houlet [19]). Fluidic or pneumatic actuation generally refers to the use of fluid under pressure to displace a flexible member (the balloon actuator by Kawai [20], the micro bellows by

Yang [21], or the osmotic actuator by Su [22]). Conversion between different types of displacement may be achieved by cascading different types of actuators, such as the flip-up sliding plate actuator by Lee [23].

Actuators can be categorized according to the type of displacement generated. Vertical displacement describes motion perpendicular to the substrate (a diffraction grating by Hocker [5], adaptive optics devices by Tuantranont [9], and Bifano [10], or a large resonant displacement mirror by Bhalotra [24]). Lateral displacement describes motion parallel to the substrate (a scratch drive actuator by Akiyama [25], a linear inchworm motor by Yeh [26], or a diffractive varying period diffraction grating by Chen [27]). Rotational motion refers to displacement about an axis, such as that generated in a micromotor (Epstein et. al. [28]). Angular displacement describes tilting [7,8]; or flip-up, (micro-XYZ stages by Fan [29] or Lin [30], a raster scanned full motion video system by Conant et. al. [31], or an automated flip-up assembly system by Reid [32]); or bending motion (switching by stress-induced bending by Chen [33]).

No fundamental limitations prevent the use of any of the above actuation methods to obtain any one of the listed types of displacement. Furthermore, large travel can be obtained for almost any combination of actuation method and displacement produced, especially if the displacement is achieved by converting one type of displacement to another, for example, using leverage. The desired application dictates the final type of displacement required, and the operational specifications (both internal and external) for the device dictate the actuation method and degree of travel.

Each actuation method has its strengths and weaknesses for different types of applications. In addition to the desired magnitude of the displacement, important metrics include speed, stability, size, and ease of fabrication. Electrostatic actuators can be very fast, stable, readily integrated with existing fabrication technology, and designed to generate various types of displacement. Thermal actuators are limited in vertical or lateral displacement, but generate large forces, so are more suited to cause bending displacement. Piezoelectric actuators generally displace by a small amount, and so they are better used to generate bending rather then vertical displacement; larger vertical travel using piezoelectric actuation typically requires excessively complicated fabrication processes or large voltages, since the displacement scales with the voltage and size of the device. Magnetic actuators often require large die area since they require coils. Fluidic actuators are typically large and relatively slow. This work focuses on actuation methods for optical applications, and this considerably restricts the set of feasible choices for actuation methods.

For optical applications there are four main types of actuators: flip-up, torsion, planar vertical, and lateral. Flip-up mirrors are used for optical benches (Lin [30], Figure 1.2a) and lateral displacement actuators are typically converted to large scale motion out of plane (Conant [31]) or large-scale planar vertical travel devices (Fan [29], Figure 1.2b). These devices enable large displacement but are not scalable into a closely packed array structure. Torsion mirrors are used to process light in reflective applications (optical add-drop switching by Ford [34] for instance) or in displays (such as the TI DMD device [7], Figure 1.3) which is particularly suited to closely spaced arrays and where light is routed depending on the mirror orientation. Vertical planar displacement of small elements allows diffractive applications (displays such as the GLV [35] or adaptive optics [9,10] for example). Lateral displacement actuators can be used to build

devices such as varying period diffraction gratings (demonstrated by Chen [27]). For reflective configurations, the type of motion of the mirrors affects the choice and size of external optics needed to collect the light; for diffractive configurations, the period of the grating and the wavelength of the incident light affect the size of the external optics, and the wavelength of the light dictates the motion required of the actuators.

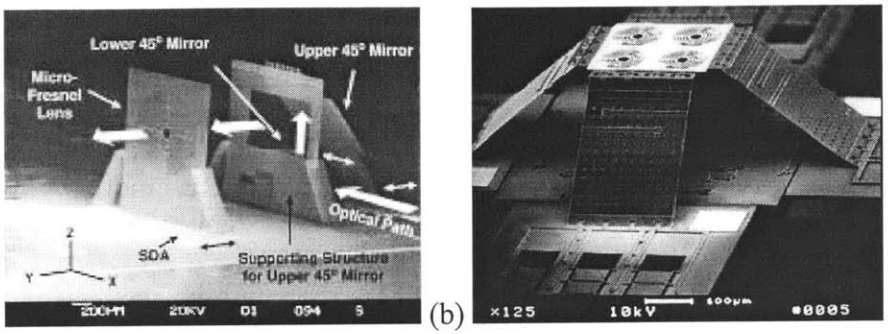

Figure 1.2: (a) Micro optical bench [30]. (b) Microactuated XYZ-stage [29].

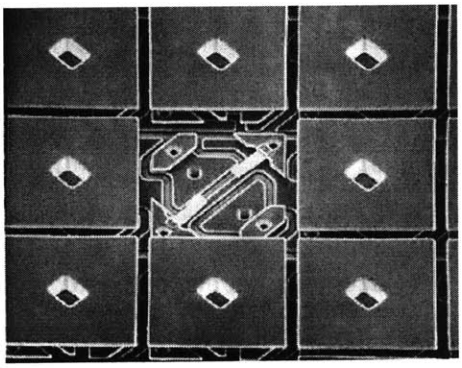

Figure 1.3: Texas Instruments DMD device (www.ti.com)

The Polychromator device discussed in this thesis must be robust, stable, and fast. Several hundred very narrow, long, closely spaced actuators must remain flat and parallel, while moving vertically relative to the substrate surface and operating at reasonable voltages. These device requirements significantly constrain the device structure and limit the choice of actuation method.

The motivation for choosing an electrostatic actuator for the near-infrared Polychromator is discussed in depth by Hung [36]. The near-infrared Polychromator structure consists of a bending beam below a flat beam and segmented electrodes, exploiting a method called leveraged bending. A simple extension of this design to obtain larger vertical displacement would require larger gaps to enable sufficient travel before the electromechanical pull-in instability. This increase in gap would, however, significantly increase the required operating voltage. Two methods to reduce the operating voltage are to use thinner beams to reduce the elastic restoring force of the beam, and a continuous electrode to increase the electrostatic force between the beam and an underlying electrode.

Another method to reduce voltage is to use shaped electrodes. This technique, described by Wagner [37], uses gray-scale lithography to etch a sloped surface, or gradual electroplating to build up a sloped surface. The sloped surface can be formed to be closer to the actuated element, thereby decreasing the operating voltage. The main drawbacks behind this approach are that the sloped surface must be planarized, the sloped surfaces are difficult to fabricate, and the sloped electrodes can take up significant area.

As noted above, Hung [36] discusses a method to increase travel using the leveraged-bending concept, which extends the range of displacement past the electromechanical instability, by using segmented electrodes positioned nearer to the supports than to the midpoint of a beam segment. The leveraged bending design increases the vertical displacement at the expense of increasing the actuation voltage. For the desired displacement in the mid-infrared Polychromator, the leveraged bending design would correspond to a prohibitively large operating voltage range. Burns [38] discusses a nonlinear flexure design in which a main cantilevered flexure contacts an auxiliary doubly supported element, which increases the stiffness and travel of the device. This design increases the vertical displacement at the expense of increased actuation voltages. Implementing the design would entail additional process complexity, such as additional polysilicon and oxide layers, if it were to enable the desired displacement for the mid-infrared Polychromator.

The two-tiered beam concept (the lower beam bends and the upper beam remains flat) is very versatile, and a variety of other actuation methods (piezoelectric, thermal, or magnetic), can be used to cause the lower beam to bend. Kawabata [16] describes a micro-scanner in which an integrated piezoelectric thin film bends a mirror out of plane. This actuation principle could be used to bend the lower beam and cause vertical motion (up or down) of the center of the beam element. An actuator based on this principle does not become unstable like an electrostatic actuator so vertical dimensions would be less and the device could travel the entire gap. Fabrication of the piezoelectric elements with additional polysilicon processing, however, would add significant process complexity.

Tuantranont [9] describes a bulk micromachined piston type mirror with a 2 to 3.5 micron vertical displacement capability, designed for adaptive optics. The square device is suspended by thermal multimorph flexures at each corner, which curl due to ohmic heating of multilayer films, each of which has a different coefficient of thermal expansion. A linear actuator could also be designed using this actuation principle. Thermal multimorph flexures would be used to bend the lower beam of the two-tiered structure. Both actuation methods, while feasible, would considerably complicate fabrication, be difficult to achieve the desired packing density, and would lack the microsecond speed of an electrostatic actuator.

Liu [18] describes a magnetic actuator designed such that a surface micromachined coil causes the bending of a plate that is connected to the substrate by cantilever beams. This technique can be used to cause bending or vertical motion directly. The coil in this work is fabricated on the moving plate, but could be fabricated on the substrate. This magnetic coil, if integrated with a lower bending beam and a flat upper beam, could provide the necessary vertical displacement, but the coil size would limit the lateral dimensions of the grating elements. In addition, the magnetic coils would complicate fabrication and introduce topography for the upper layers.

Electrostatic actuation comes closest to fitting the combination of desired features for the mid-infrared Polychromator, without significant fabrication complexity, and was therefore chosen as the method to achieve large vertical travel.

1.2 Thesis Outline

This section provides an overview of the material discussed in this work. In the present chapter, previous work on the near-infrared Polychromator device is presented as background for the work presented in the thesis. The motivations for extending the range of operation of a programmable diffraction grating from its initial configuration in the 3 to 5 micron wavelength range, to operate in the 8 to 12 micron wavelength range and the device specifications are described. Finally, the work done for this thesis is summarized.

Chapter 2 presents the parameters and constraints affecting device design and the simulations used to demonstrate the functionality of the device. A simplified but illustrative energy method model, a more accurate idealized finite difference method (FDM) model, and a more detailed structurally exact model are used to simulate device designs and predict performance. Two design challenges that were overcome in this work, end effects and support compliance, are addressed, and the discussion highlights the interaction between design and fabrication.

The fabrication of the device is discussed in Chapter 3, encompassing device layout and the process flow, and is illustrated using device cross-sections. The development of key process steps to build tall structures is also discussed. Fabrication challenges including metalization, release, and packaging are addressed. The results of the fabrication process are then presented.

The experimental results of this thesis are presented in Chapter 4. The method of experimental testing of displacement is described. Beam displacement characteristics for several fabricated designs are measured, and the designs are then compared to models to estimate the stress in the devices. The results are compared to full simulations based on the extracted stress, and show excellent agreement. The measurement repeatability of a single element, the reliability over many actuated cycles, the uniformity of actuator performance across the device, and the device yield is reported using data collected by an automated measurement system.

Chapter 5 describes the scalability of the design and concludes with a brief discussion of the work presented in the thesis and future work that could be based on this device.

1.3 Near-infrared Polychromator

The Polychromator project is a collaboration between the Massachusetts Institute of Technology, Sandia National Laboratories, and Honeywell Laboratories. The spectral synthesis, optical system fabrication, and experiments to demonstrate gas detection were performed at Sandia Labs. The majority of the fabrication and process development was performed at Honeywell Labs. Electromechanical design, simulation, part of the fabrication and process development, and testing was performed at MIT.

The near-infrared Polychromator diffraction grating, discussed as background for this thesis, was designed to process light in the 3 to 5 micron spectral window. The elements of the diffraction grating were designed to achieve 1.5 to 2 microns of planar vertical travel in a low tensile stress polysilicon surface-micromachining process. The design includes several notable design features such as leveraged bending and a two-layer beam structure, and is capable of actuation to almost the full gap with planar vertical displacement. The fabrication of the device employs a custom, 11 mask fabrication sequence, which does not significantly differ from currently available standard fabrication processes. The fabricated structures exhibited the desired actuation and optical characteristics.

1.3.1 Device Design

The deflection of each element is a function of the applied voltage, and the maximum travel is limited by an electromechanical instability called pull-in [39]. Stable displacement is maintained upon increasing voltage until pull-in; at pull-in, the beam snaps to the underlying electrode, after which the system no longer has a point of stable equilibrium, and in most cases is a critical device failure. For the beam lengths and widths used in this design, and for a beam thickness comparable to the free-space gap, actuation via a continuous underlying electrode results in pull-in when the lower beam is displaced by approximately one-third of the free-space gap. To achieve positioning beyond the pull-in instability, the design of the Polychromator device takes advantage of leveraged bending [40]. The grating element design shown in Figure 1.4 and Figure 1.5 uses a two-beam structure attached periodically to the underlying layer, in which the lower beam undergoes bending while the top mirror beam deflects vertically without flexion.

Applying voltage to the segmented actuation electrodes located near the support posts allows leveraged bending of the lower beam and controllable positioning of the upper mirror beam through the full gap. Electromechanical analysis tools are used to help design structures capable of near-full-gap actuation with voltages of about 100 volts or less. The gaps and beam thicknesses are about 2 μm. For the near-infrared devices, post-to-post spacings (*B*) are in the range of 500 to 700 μm, and electrode lengths (*E*) are in the range of 80 to 100 μm.

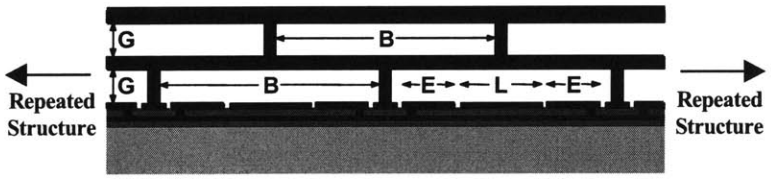

Figure 1.4: View of the unactuated Polychromator grating beam structure in cross-section (B is the doubly-supported beam length, E is the length of one segmented actuating electrode, L is the ground pad length, and G is the lower and upper free-space gap).

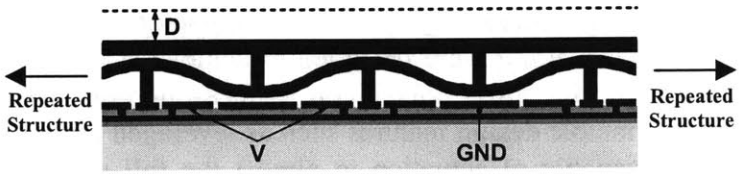

Figure 1.5: View of beam structure in cross-section when actuated. The lower beam undergoes bending, while the top mirror beam remains flat and deflects vertically (D is the vertical displacement from the original position when voltage V is applied to the actuating electrodes).

1.3.2 Fabrication Process

The near-infrared Polychromator grating device is a combined Honeywell-MIT fabrication effort, using polysilicon surface micromachining. Two polysilicon layers are used to create the actuated structure, and two more are used for electrical interconnections and actuating electrodes. The process begins with growth of a thermal oxide on an ultra-flat silicon wafer. Two layers of boron-doped polysilicon, separated by silicon nitride, are used for the interconnection and electrode structures. Next, a sacrificial silicon dioxide (SiO_2, or simply oxide) layer is deposited, which will define the actuation gap. Support posts for the bending layer of polysilicon are patterned and etched in this oxide layer. Before the deposition of the bending layer of polysilicon, small dimples are also etched in the oxide. The dimples cause nodules to form on the bottom of the polysilicon layer; these nodules help prevent stiction during operation, should the bending beam pull in. The bending layer of polysilicon is then deposited, implanted, and patterned, and the second sacrificial oxide layer is deposited. The second oxide layer has vias etched in it to create support posts for the polysilicon mirror beam layer. The polysilicon mirror-beam layer is then deposited, implanted and patterned. Typical thicknesses for the bending and mirror beam layers of polysilicon and for the two sacrificial oxide layers are approximately 2 μm. The wafers are then annealed to reduce the polysilicon stress. The process is completed with the deposition of gold onto the mirrors and pads and the removal of all of the sacrificial oxide. The fabricated element and grating are shown in Figure 1.6 and Figure 1.7.

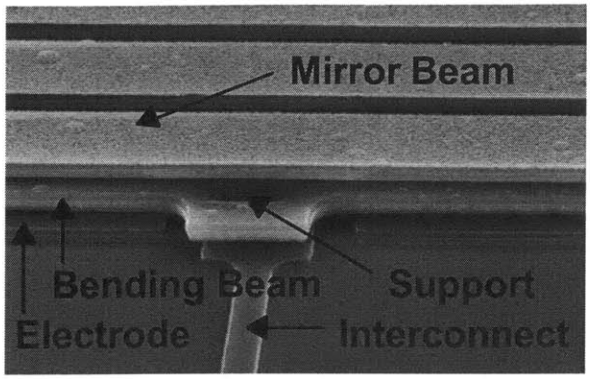

Figure 1.6: SEM of grating showing the double beam, support structure, interconnects, and electrodes [5].

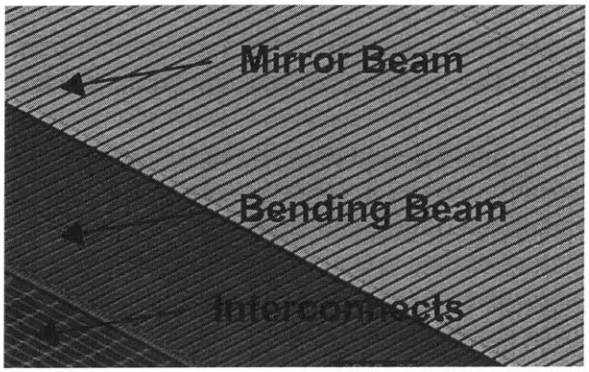

Figure 1.7: SEM of the edge of a MEMS Polychromator grating showing interconnects, lower bending beam, and upper mirror beam. Beams are 10 microns wide and 1 centimeter in length [5].

1.3.3 Device Operation

The individual diffractive elements of the Polychromator grating are actuated electrostatically. Beam deflection depends primarily on the applied voltage, electrode length, distance between support posts, beam thickness, residual stress, and free-space gap. Combinations of mask design and process parameters are selected to result in structures that maximize travel while requiring only moderate actuation voltage. To evaluate fabricated devices, interference microscopy is used to measure vertical movement of individual beam elements as a function of applied voltage, such as by Volpicelli [41] or by Bardhan [42]. Results for several grating element designs are shown in Figure 1.8. Measured maximum beam deflections for these devices are nearly the full gap of two microns, and pull-in occurs at voltages ranging from 65 to 110 volts, depending on the particular device design.

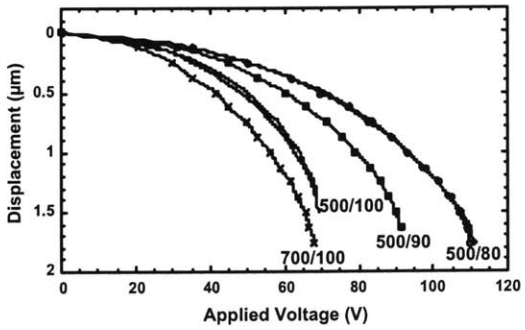

Figure 1.8: Displacement versus actuating voltage for a variety of grating element designs (numbers in the figure indicate the beam length to electrode length relationship B/E in Figure 1.4 in microns for each design) [5].

To minimize packaging complexity, the first devices fabricated used only 132 pads for signal and ground; this decision allowed integration with a readily available pin-grid-array package (Figure 1.9). In order to actuate all 1024 lines with this limited input/output capability, the grating elements are hard-wired on-chip as 8 repeat units of 128 elements. In this configuration, a voltage applied to a bond pad actuates 8 grating elements, one from each repeat unit. This on-chip hard wiring, while advantageous for device packaging and initial testing, has a deleterious effect on device yield; if any one of the eight lines connected to a pad is compromised, none of the eight elements in that set will function. Despite the drawbacks of this configuration, successful synthetic spectra have been demonstrated (Figure 1.10) and optical results have been obtained (Figure 1.11) [5].

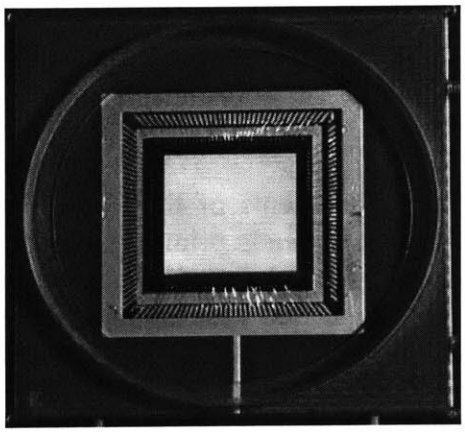

Figure 1.9: Packaged Polychromator die. Array is 1 cm x 1 cm [5].

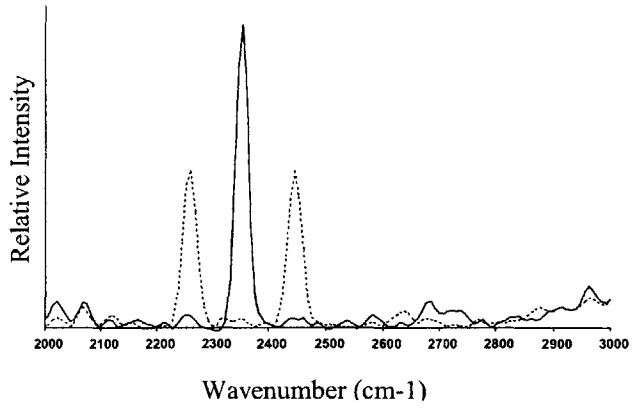

Figure 1.10: Spectral transmission of the near-infrared Polychromator for the two grating profiles used for CO_2 detection. The solid line spectrum matches the CO_2 absorption at 2350 cm^{-1}, while the double-bandpass dashed line spectrum samples an equal area outside the CO_2 absorption [5].

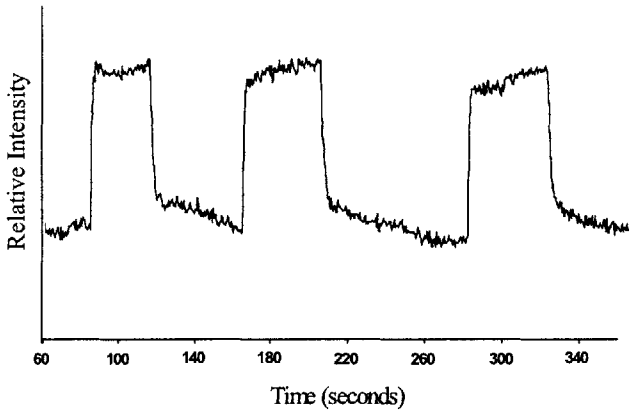

Figure 1.11: Response of the correlation spectrometer to 100 ppm-meters of CO_2 admitted and purged from a gas cell 3 times [5].

1.4 Mid-Infrared Polychromator

The mid-infrared Polychromator diffraction grating is designed to process light in the 8 to 12 micron spectral window. Processing light in this wavelength range requires altering several features from the previous near-infrared design, including the beam width, the target vertical displacement, and the number of elements. Other features, such as the length of the elements, and the space between elements, remain essentially unchanged. The design choices are outlined in this section and the resulting specifications for the device are presented.

The overall optical system is governed by the diffraction angle of the device. The larger the diffraction angle can be set, the more compact the optics are and the easier it is to put the optics around the device. The diffraction angle of the grating is set by the diffraction grating formula, $\theta = \sin^{-1}\left(\lambda/d\right)$, where λ is the wavelength of interest and d is the minimum period of the grating. The minimum period of the grating occurs when

every other beam is displaced and is thus twice the pitch of the grating. In order to effectively diffract light at one observation angle and create spectra in the region of interest, it is necessary to set the diffraction angle smaller than the diffraction angle for the smallest wavelength. The width of the beams directly affects the diffraction angle; the wider the grating elements are, the smaller the diffraction angle will be.

The algorithms designed by Sinclair et al. [4] to reproduce the desired spectra are based on scalar diffraction theory. In order for these models to be valid (so that analysis may avoid the use of vector diffraction theory, which would be significantly more computationally intensive) the beam widths should be wider then the longest wavelength of interest. In order to satisfy the constraints on diffraction angle and diffraction theory the width of the elements were chosen to be 20 microns.

The models used by Sinclair to generate the synthetic spectra use Fourier analysis to determine the vertical position of the diffractive elements. The analysis requires that, for optimal spectra, the beam be capable of sufficient displacement to induce a phase shift of 2π. For this phase shift (corresponding to a vertical beam displacement of $\lambda/2$) the desired wavelength range necessitates 4 to 6 microns of planar vertical travel. It is possible to generate spectra with less travel, but the resolution and efficiency of the grating will be degraded. The reproduced spectra may have the wrong relative intensities of the features in the desired spectrum, as well as washed out spectral features of the desired spectra, as the maximum achievable displacement is decreased.

The number of beams directly affects the resolution of the device, which is the ability to resolve or reproduce a desired spectral feature. The resolution is given by: $\lambda/\Delta\lambda$, which scales directly as: $\#Beams/2$. Therefore, as the number of beams on a device decreases, the spectral resolution decreases proportionally. For the spectra of interest in the mid-infrared region, a resolution of about 250 is sufficient, so the number of elements was chosen to be 512.

The main factor determining the optical efficiency of the grating is the ratio between the width of the grating element and the space between elements. As this ratio increases, the grating becomes increasingly efficient, because more light is diffracted and less light is lost, or scattered, by the spaces. Therefore, increasing the elements' widths or decreasing the space between elements increases the efficiency of the grating. The minimum space is limited by the available process technology minimum feature size of two microns for the mirror layer.

The length of the elements may be chosen somewhat arbitrarily. The decision for the element length is based on keeping the optics relatively simple by having a square optical area. The length of the elements, without using cylindrical optics, is equal to the width of the device. The lengths of the elements are thus the pitch of the elements multiplied by the number of elements, and the pitch of the grating is defined to be the width of one element plus the space next to it.

In order to operate in the wavelength range of interest and successfully build devices given the complexity of achieving the desired travel, devices that achieve between 4 and 6 microns of travel are designed. The fabrication technology used has a minimum feature size of two microns, and the space between grating elements is set to this size, to maximize diffraction efficiency. The widths of the elements are chosen to be 20 microns so that the diffraction angle of the device is not too small and the optical

theory is within the scalar diffraction limits. By using 512 elements and a pitch of 22 microns, the width of the device is 1.1 centimeters; this also then determines the length of the elements. The minimum first order diffraction angle with a period of 44 microns is just over 10 degrees, which does not overly complicate the optics external to the device. It should be noted that none of these parameters is independently essential to the device performance; rather, it is the combination of parameter choices that results in effective device performance.

1.5 Summary of Work of This Thesis

The mid-infrared design created for this thesis was based largely on the near-infrared design described above. The design process focused on meeting the new specifications, while implementing design and process simplification, and improving manufacturability. The process complexity was reduced by using three layers of polysilicon instead of four, as in the previous design. A nitride spacer, used as a critical insulator in the near-infrared design, was not robust to manufacturing; it was therefore subsequently designed out of the process by redesigning the beam support structure, highlighting one of the focuses of the thesis – the mutual dependence between structure design and fabrication sequence.

In Hung [36], the nonlinear spring effect was demonstrated in the near-infrared leveraged bending prototype structure. The fabrication process of these devices limited the upper gap to 0.6 microns, at which point the upper beam contacts the lower support posts. As voltage is increased, the experimental results of the stiffer two-beam structure deviate from simulations, which predict nearly full travel of the lower beam segment (Figure 1.12). The configuration did not allow full voltage-displacement testing of the prototype device. This limitation was turned into a critical enabling feature of the current design, and is called the multi-layer nonlinear spring (MLNLS) (Section 2.1). Hung suggested using the stress-stiffening concept to achieve large travel [36]; simulations of devices exploiting stress stiffening were used to explore the design space, and indeed, a design window that could exploit this concept was identified and used here. Several designs that met the goals of large displacement in simulation were fabricated and tested.

Initial modeling of the multi-layer nonlinear spring concept was performed using an energy method analysis (Section 2.2.1), which balances the stored energy in the displaced beams with an electrostatic force. This technique allowed rapid exploration of the design space by using analytical expressions for the relation between design variables and performance metrics. Since this was a very approximate calculation, more exact simulations were conducted with two focuses: displacement characteristics, and pull-in protection. The displacement design space was mapped as a function of the most significant design and process variables (beam length and free-space gap) using a modified version of FDM code from previous work by Hung [36] (Section 2.2.2). The pull-in protection was simulated using the MEMCAD 4.8 software [43] (Section 2.2.4). An ideal beam was also modeled using MEMCAD to validate the FDM simulations (Section 2.2.5). Deleterious end effects encountered in the near-infrared design were analyzed, and eliminated using tethers to compensate for stress imbalances (Section

2.3.1). Careful consideration was given to support design, given the height of the supports and the stress in the polysilicon (Section 2.3.2).

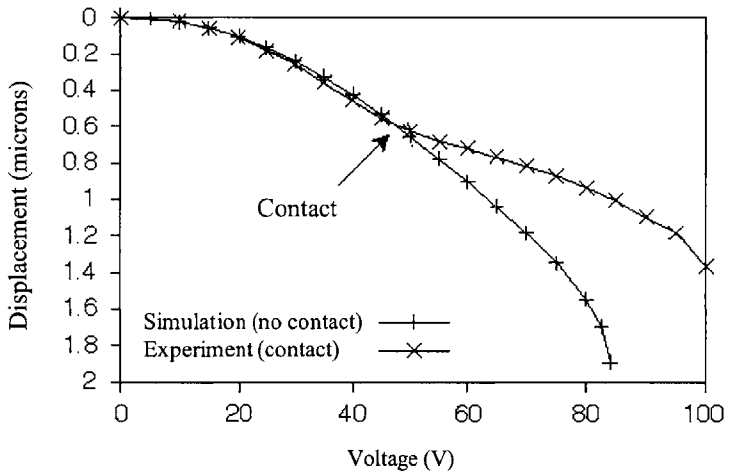

Figure 1.12: Plot of displacement versus voltage for prototype near-infrared device using a limited process such that the upper beam segment only moved down 0.6 microns before contact [36].

Two fabrication processes were developed in collaboration with the Honeywell team to enable large travel; the first (Section 3.1.1) suffered from fabrication difficulties, but the second (Section 3.1.2) succeeded in producing functional devices (Section 3.3). A robust thick oxide deposition strategy was developed that enabled the fabrication of the large gaps necessary for the design (Section 3.2.1). Effectively, a fabrication process was developed around a design concept, and then the fabrication process suggested a new design concept, which simplified the fabrication process.

The completed structures are tested using an interference microscopy-based testing system, set up by Bardhan [42] (Section 4.5.1), by imaging optical fringes on a tilted sample. This can be used to map a fringe shift to a vertical displacement, as voltage is applied to a diffractive element. Experimental results from different devices on the same wafer enabled the estimation of the residual stress; the consistency of the estimated stress value from devices with varying beam lengths validated both the models and the experimental results (Section 4.4.1). The full experimental device behavior showed excellent agreement to the simulation of the full device structure as modeled using the MEMCAD software (Section 4.4.2). The automated system enabled determination of repeatability, reliability, uniformity, and yield (Sections 4.5.2–4.5.5). Successful devices are now being incorporated into bench-top Polychromator systems for spectroscopic evaluation by the sponsoring agency.

Chapter 2: Design and Simulation

This chapter describes the design of the mid-infrared Polychromator and the simulations used to model the design. In order to generate synthetic spectra in the 8 to 12 micron wavelength region the diffractive elements should travel approximately 6 microns. If the leveraged bending near-infrared design were simply scaled up to allow 6 microns of displacement, the required actuation voltage would be prohibitively large (in the range of several hundreds of volts). If the beam lengths are increased significantly to reduce actuation voltage, the yield could deteriorate due to process difficulties such as buckling or stiction. However, if a single electrode is used under a doubly supported beam and the thickness of the beam is decreased as the gap is increased, the beam enters a regime of stretching rather than bending [40]. Stress stiffening increases the achievable travel from one-third of the gap to just over half of the gap. This simple doubly supported beam design (Figure 2.1) is, however, susceptible to pull-in unless the travel is limited. In the MLNLS design, the upper mirror beam is used to stiffen the lower actuating beam (Figure 2.2), increasing the pull-in voltage and travel of the two-beam combination and thus performing this limiting function. This multi-layer nonlinear spring (MLNLS) design is introduced, and design parameters (Section 2.1.1) and constraints (Section 2.1.2) that limit the design are discussed.

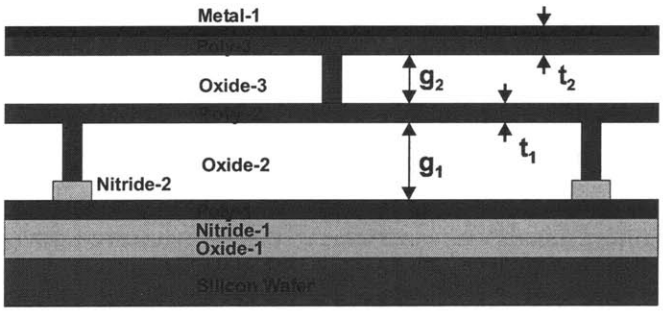

Figure 2.1: Polychromator beam structure in cross-section for the unactuated state (g_1 is the lower gap and g_2 is the upper gap, t_1 is the actuating beam thickness and t_2 is the mirror beam thickness).

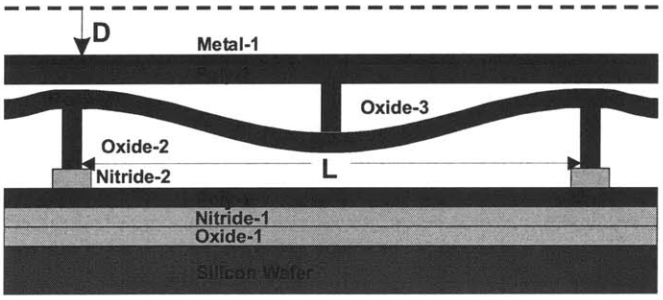

Figure 2.2: Beam structure in the actuated state. The lower beam segment of length, L, undergoes bending, while the top mirror beam remains flat and deflects vertically, distance D, when voltage is applied to the actuating electrode.

Several methods for modeling Polychromator designs were used for different purposes and each is presented here. Energy method analysis (Section 2.2.1) provides an analytical model of the device behavior and allows rapid insight into the design space. Finite difference method (FDM) simulations (Section 2.2.2) are then used to more accurately determine lower beam travel and actuation voltage. From FDM simulations, a set of designs can be found to span the design space that meets the constraints of fabrication and actuation voltage. The MEMCAD software (Section 2.2.4) is used for full 3-D electromechanical simulations of the set of designs, using contact boundary conditions and more exact structural geometry, and thus provide more accurate modeling tools of critical design features. Experimental results can be compared to the MEMCAD simulations, so that device performance can be quantifiably analyzed against computational predictions.

End effects in the grating elements were observed in the near-infrared Polychromator that caused pull-in prematurely (at a lower travel than predicted). A model of the shape of the end of an element matched experimental results. New designs were created to avoid this problem and then simulated to ensure that the effect had been eliminated. The new design, once fabricated, did not suffer from the previously observed failure mode. This is a good example of the interaction of the design and fabrication processes required to realize the device. Support compliance was known to be a problem in the near-infrared devices, and was expected to have even more significant effects in the mid-infrared devices because the supports are taller. To understand support compliance effects, a significant quantity of modeling was done prior to fabrication of the mid-infrared devices. Supports were designed to be robust by balancing the stress being applied to them.

2.1 Multi-layer Nonlinear Spring Design

The operation of this device is similar to the near-infrared device: a lower bending beam, which is attracted to a lower layer by an electrostatic field, displaces a flat beam vertically. The process has been modified so that only three layers of polysilicon are required (Figure 2.1 and Figure 2.2). Replacing the interconnect and electrode layers from the near-infrared design with one layer that provides both functions reduces the complexity of the design, and eliminates the electrical shorting behavior between the layers observed in crossovers required in earlier designs. Isolation between the electrodes and beam posts is created by adding insulating nitride at the supports (as in Figure 2.1) or by having segmented or lateral supports (Figure 2.24b and Section 3.1.2) so that the electrode can continue beneath it. When the nitride insulation is used, the supports and nitride insulation are recessed (Section 3.1.1) to minimize topography in the beams and mirror layers. Several key design parameters in both layout and process must be chosen, subject to design constraints, to enable the desired displacement.

2.1.1 Design Parameters

In order to achieve the desired upper beam actuation, several parameters must be chosen in the layout and process: beam segment length, electrical isolation method, and film thickness (Figure 2.1). The beam length is the most important factor in choosing the layout parameters. As beam segment length increases, the pull-in voltage decreases, and fabricating functional devices becomes more difficult due to processing problems such as stiction during release. There is also a slight decrease in the stable vertical travel (prior to pull-in) of the beam for longer beam lengths.

Electrical leakage or cross-talk between adjacent electrodes can occur when applying high voltages to the device. To try to prevent these effects, a grounded spacer in the electrode layer that runs between the electrodes, as well as a larger space between electrodes, were included in some designs. These features had not been included in the near-infrared Polychromator, so some mid-infrared designs included this feature to test the effect of this modification. The decreased width of the electrodes increases the pull-in voltage but can prevent electrical device failure.

Given a beam segment length, the thickness of the deposited films determines the functionality of the device. Actuation voltage and total displacement before pull-in are determined by the choice of the lower gap g_1 and the actuation beam thickness t_1 (Figure 2.1). If the lower gap is increased, a larger voltage is necessary to actuate the beam to a given displacement, and the maximum travel is increased. If the lower beam thickness is increased, the beam will have a higher pull-in voltage at a marginally decreased maximum displacement. The upper gap g_2 and the mirror beam thickness t_2 are designed to limit the travel of the lower beam by permitting the upper beam to contact the supports of the lower beam. This contact – designed to occur before the pull-in instability point of the lower beam alone – creates a stiffer two-beam structure that requires more voltage to displace it beyond the "touchdown" displacement than if the lower beam were actuated alone. This nonlinear spring effect prevents catastrophic pull-in, shorting, and possible device failure, by increasing the stability of a non-stiffened beam before it becomes unstable. The upper gap must be less than the stable displacement of the lower beam, so that the lower beam is stiffened before the pull-in instability is reached. To maximize travel and pull-in protection, the upper gap should be 70 to 90 percent of the expected travel before pull-in, which corresponds to an upper gap thickness that is about half of the lower gap thickness. The mirror beam thickness determines the stiffness of the two beams after contact. The thicker the mirror beam is designed, the stiffer the new spring becomes, requiring a larger voltage before the two beams eventually reach pull-in. However, as explained in Section 2.3.1, a thicker upper beam aggravates an end-effect which required redesign to permit stable operation while maintaining flatness across the optically accessed section of the device.

2.1.2 Design Constraints

There are three main constraints on the design: the available voltage range, the mask requirements, and the process technology. The dielectric properties of the thin films used in the fabrication of the device, such as dielectric constant, breakdown voltage,

surface leakage, and dielectric film quality, effectively limit the voltage range to below 130 Volts. The type of electronics used also limits the voltage range. For the near-infrared Polychromator a 128-channel voltage source with a 0 to 200 Volt range was developed [44]. For bench top demonstration systems a 512-channel 150 Volt voltage source was developed. For eventual integration into an ASIC voltage driver, designs with less than 80 Volts actuation are desired. The constraints on the mask design include the minimum feature size (two microns), the size of the desired active optical area (approximately one square centimeter), and the interconnects and bond pads necessary to apply voltages to the chip. The process technology constrains the thickness of each layer. A thin layer (less than one micron) may not be mechanically robust enough to function correctly, but a thick layer (poly more than 2-3 microns, and oxide more than 4-5 microns) is more difficult to fabricate since thick films are prone to cracking. A thick layer is also more difficult to pattern and etch. Achieving the desired geometric properties is also more difficult. The film stress is one of the most important factors in processing. If a film is compressive, the beams will buckle and be mechanically useless. For tensile stress, as the residual film stress in the beam increases, the actuation voltage required for a specific beam displacement increases and the displacement at pull-in decreases. In order to maximize travel and minimize voltage, it is desirable to have a very slightly tensile film stress, in the range of 5 to 15 MPa.

In order to achieve six microns of travel the lower gap must be approximately 12 microns. This is very aggressive for a surface micromachined process, and so process variations with various thicknesses were fabricated in the initial processing run to validate the voltage-displacement models and the MLNLS effect, and to push the limits of fabrication. The designs have lower gap thicknesses of 6, 8, 10, or 12 microns. The beam thickness was chosen to be 1 micron for all designs. As explained in Section 2.3.2, if beams are thinner than 1 micron, the supports will not be structurally rigid. If beams are thicker than 1 micron, the actuation voltage will be too high. The upper beam was chosen to be at least two microns thick, but could be thicker if fabrication allowed. In order to test several designs for a range of processing conditions, the mask contains a set of designs with different beam segment lengths. These range from 600 to 1200 microns: below 600 microns, the actuation voltage would be too high, and above 1200 microns, beams would not be mechanically reliable. Given these bounds on the design parameters, it was necessary to find a parameter space that would perform within the given constraints. The role of simulation was to help find a reasonably tight bound on the parameter space in which devices would perform to the desired specifications.

2.2 Simulation

Three types of simulations are used to describe and analyze the multi-layer nonlinear spring (MLNLS) design. Energy method analysis allows rapid insight into the design space by providing an estimate of the device functionality. Finite difference methods (FDM) allow more accurate modeling and are used to characterize the displacement of the lower beam as a function of beam segment length and free-space gap for an ideal doubly supported beam; FDM analysis is also used to investigate the effects of stress on the design. MEMCAD simulations provide the most accurate modeling of the techniques and are used to simulate the full two-tiered beam structure - in particular,

the critical MLNLS design feature, exact structural geometry, and non-ideal boundary conditions. The three modeling techniques are compared using an ideal structure to quantify the differences between each simulation tool and validate the use of FDM simulations for device design.

2.2.1 Energy Method Analysis

MEMS devices are well suited to energy method analysis since the systems conserve energy [45]. In equilibrium, the energy stored in the system will equal the work done to the system. In an analysis of a doubly supported beam with an underlying electrode, the stored energy arises from the bending and stretching of the beam under a uniform load. The work done by the external load is the force of attraction multiplied by the change in displacement between the beam and electrode. In energy method analysis a trial function is chosen to represent the shape of the deflected beam. Depending on the residual stress in the beam, a cosine or exponential estimates the shape accurately enough to get meaningful results for several microns of displacement; beyond this threshold, the approximated beam shape no longer accurately models the deformed beam.

In the following description a cosine beam-shape trial function is used (Eqn. 1). The beam segment length is L, the center displacement is d, and $v(x)$ is the amount of vertical displacement of the beam at each position x on the beam (Figure 2.3). The beam is centered at zero and the ends are fixed at $\pm L/2$.

$$v(x) = -\frac{d}{2} \cdot \left(1 + \cos\left(\frac{2 \cdot \pi \cdot x}{L}\right)\right) \tag{1}$$

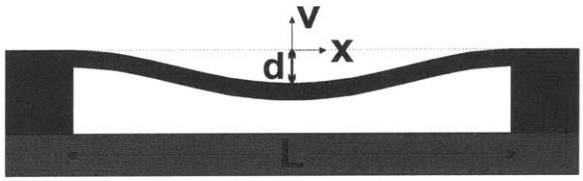

Figure 2.3: Cross-section of beam-shape and reference point for a model of an ideal doubly supported beam.

Once the total axial strain from bending and stretching of the beam is integrated over the entire beam, the total strain energy and the potential energy in the system can be found. Differentiating the expression for the potential energy with respect to the displacement, setting the result to zero, and solving gives an expression for the load on the beam as a function of its center deflection [45]. In the two-beam structure the bottom beam experiences an approximately uniform distributed pressure load, q, over the entire beam resulting from an electrostatic force between the beam and the underlying electrode (Eqn. 2) (Figure 2.4a). The top beam at contact experiences a point pressure load, P, in the center of the beam where the two beams are connected (Eqn. 3) (Figure 2.4b). For an extra change of displacement after contact, more elastic energy is stored in the beam structure, since the mirror beam is bending also; equivalently, the structure is a stiffer

spring. In the following equations, E is the Young's modulus of polysilicon, σ_0 is the axial residual stress, t_1 and t_2 are the thicknesses of the lower and upper beam, and g_2 is the height of the upper gap.

$$q = \frac{\sigma_o \cdot t_1 \cdot \pi^2}{L^2} \cdot d + \frac{E \cdot t_1^{\,3} \cdot \pi^4}{3 \cdot L^4} \cdot d + \frac{E \cdot t_1 \cdot \pi^4}{4 \cdot L^4} \cdot d^3 \tag{2}$$

$$P = \frac{\sigma_o \cdot t_2 \cdot w \cdot \pi^2}{2 \cdot L} \cdot (d - g_2) + \frac{E \cdot t_2^{\,3} \cdot w \cdot \pi^4}{6 \cdot L^3} \cdot (d - g_2) + \frac{E \cdot t_2 \cdot w \cdot \pi^4}{8 \cdot L^3} \cdot (d - g_2)^3 \tag{3}$$

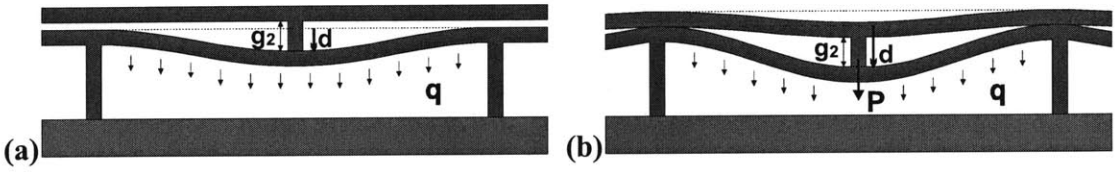

Figure 2.4: Force on two beam structure (a) before and (b) after contact

The resulting force of the uniform pressure load on the beam is the pressure load multiplied by the area of the beam. Before the upper beam makes contact, the force on the lower beam is given by F_1 (Eqn. 4). Once the upper beam makes contact with the support posts, the beam has both a uniform pressure load and a point pressure load component, and the force on the lower beam is given by F_2 (Eqn. 5).

$$F_1 = q \cdot A \qquad (d<g_2) \tag{4}$$

$$F_2 = q \cdot A + P \qquad (d>g_2) \tag{5}$$

These two forces represent the elastic restoring force of the beam, which is counteracted, by the electrostatic force of attraction F_{elect} between the beam and underlying electrode (Eqn. 6). In this equation ε_0 is the permittivity of free space, g_1 is the initial lower gap, and V is the applied voltage. The force of actuation is approximated as a uniform pressure load using a parallel plate capacitor with a spacing at the middle of the segment. This approximation is removed in the FDM and MEMCAD simulations..

$$F_{elect} = \frac{\varepsilon_o \cdot A \cdot V^2}{2 \cdot (g_1 - d)^2} \tag{6}$$

For the analysis in this subsection, the lower beam segment length L = 600 μm, the lower beam thickness t_1 = 1 μm, the upper beam thickness t_2 = 4 μm, the lower gap thickness g_1 = 8 μm, and the upper gap thickness g_2 = 3.5 μm, (as defined in Figure 2.1 and Figure 2.2). The Young's modulus, E = 160 GPa, the residual stress, σ_0 = 15 MPa, and the beam and electrode width, w = 20 μm. In a plot of force versus displacement, the intersections of Equation 4 or 5 with 6 for a variety of voltages describe the possible solutions to the equations (Figure 2.5). When there are two points of intersection, shown

as white and black circles on Figure 2.5, one white circle describes a stable solution to the equations, at the lower displacement, and the black circle is an unstable solution. When voltage is applied to the beam, the electrostatic curve moves up and to the left; the locus of stable solutions is shown. The pull-in voltage occurs at the point when the curves of electrostatic and restoring force are tangent to each other, shown as a gray circle on Figure 2.5. The lower beam, if not limited by the upper beam, reaches pull-in at $V_{PI,1}$ = 116 Volts when the electrostatic force, F_{elect}, is tangent to the restoring force, F_1. The upper beam contacts the supports of the lower beam after the lower beam travels 3.5 microns, as shown in Figure 2.6. The restoring force of the two beams, F_2, is tangent to the electrostatic force, when $V_{PI,2}$ = 145 Volts is applied. The stiffer multi-layer beam thus increases the pull-in and travel of the device. This figure shows the multi-layer nonlinear spring effect, which provides the pull-in protection and is one of the main design features of the mid-infrared Polychromator.

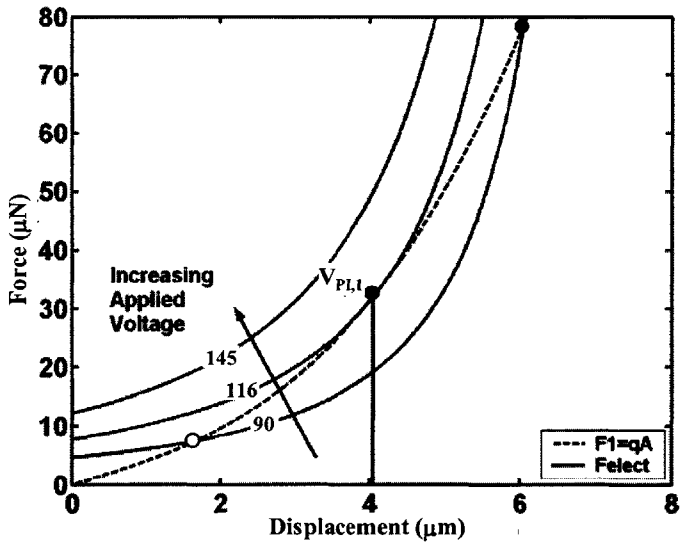

Figure 2.5: Force versus displacement for a stress stiffened doubly supported beam without the MLNLS.

To find the displacement of the beam as a function of applied voltage, the equation for the electrostatic force (Eqn. 6) is solved for the voltage as a function of the force. The restoring force of the beam, F_1 when $d < g_2$, and F_2 when $d > g_2$, can then be inserted into this equation resulting in two expressions for V as a function of d (Eqn. 7 and 8). At contact when $d = g_2$, the two forces are equal ($F_1 = F_2$). The displacement, as a function of voltage, is plotted in Figure 2.7, and the maximum displacement of the center of the beam is (g_1-d).

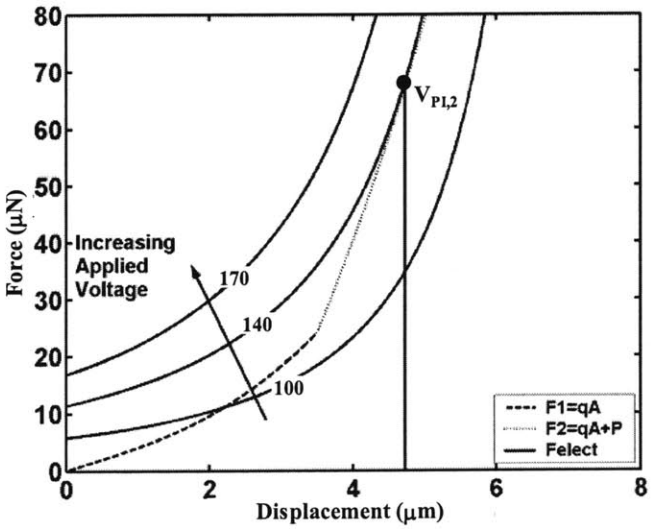

Figure 2.6: Force versus displacement for a doubly supported beam with the MLNLS effect increasing the pull-in voltage and travel of the beam segment..

$$V = \sqrt{\frac{2 \cdot (g_1 - d)^2}{\varepsilon_o \cdot A} \cdot F_1} \qquad (d<g_2) \tag{7}$$

$$V = \sqrt{\frac{2 \cdot (g_1 - d)^2}{\varepsilon_o \cdot A} \cdot F_2} \qquad (d>g_2) \tag{8}$$

A plot of travel as a function of voltage shows the characteristic transfer curve of the stress-stiffened multi-layer nonlinear spring design (Figure 2.7). The primary beam is displaced as the voltage is increased, until it has traveled the height of the upper gap (the point of contact indicated in Figure 2.7). This region of the graph shows the stable operating region when the upper beam is flat. Before pull-in of the lower beam, the upper beam contacts the posts of the lower beam and bends, effectively stiffening the lower beam. This acts to protect the device from destructive failure by increasing the stability of the structure at the maximum operating point. In the MLNLS design the device operates up to the maximum stable displacement, roughly half the gap, without the risk of catastrophic device failure should the displacement exceed this.

This analysis, although illustrative, intuitive, and computationally simple, is not accurate enough to be used to make parameter choices for fabrication. The solution is based on the trial function used to describe the shape of the bent beam. If the beam bends into a shape that is not well described by the trial function, this method will not accurately describe the transfer function between voltage and displacement. The analysis is useful though, because it provides insight into the functional dependence between design parameters and device performance. With insights from the energy method analysis, a more limited subset of the parameter space can be explored with more accurate and computationally expensive simulation tools.

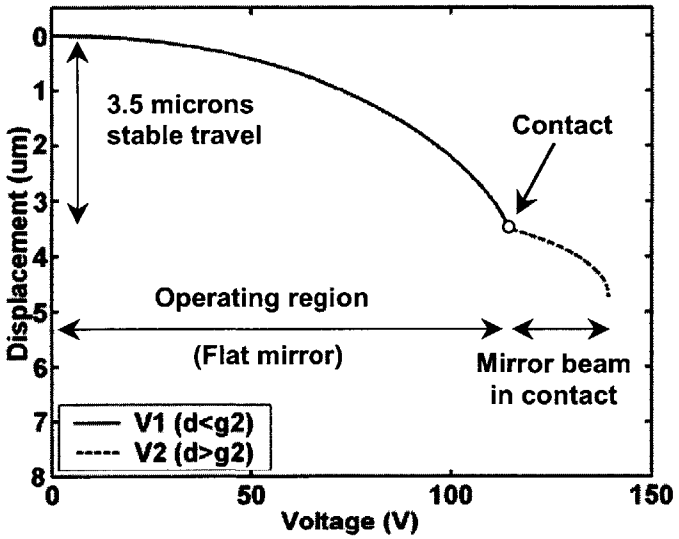

Figure 2.7: Travel versus voltage for the multi-layer nonlinear spring design.

2.2.2 Finite Difference Method Analysis

The finite difference model was developed by Hung [36] to analyze the effects of varying the electrode length in the leveraged bending design. The C code was modified for the new Polychromator design, to simulate a doubly clamped beam with a continuous electrode. The code takes as inputs the beam length, lower gap, beam and electrode width, and beam thickness. The outputs are the pull-in voltage and maximum travel of the specified design. The FDM can also generate the voltage-displacement transfer function and the deflected beam profile just before pull-in. For the analysis in this subsection, the lower beam thickness t_l = 1 μm, the beam and electrode width w = 20 μm, the Young's modulus E = 160 GPa, and the residual stress σ_0 = 15 MPa.

The lower gap has the most significant effect on the displacement characteristic of the beam (Figure 2.8). The lower gap and the beam length together have large effects on the voltage required to actuate a beam (Figure 2.9). These are the key parameters in the design. In order for devices to function within design constraints at a variety of beam lengths and lower gaps, it is important to map the design space and choose the most viable designs. The maximum travel and actuation voltage is shown in a combined contour plot, as a function of beam length and lower gap (Figure 2.10). If the regions not accessible by the drive electronics and below the minimum desired travel are ignored, the remaining region contains the designs that meet the desired specifications. Choices of beam length and lower gap are then chosen in this region.

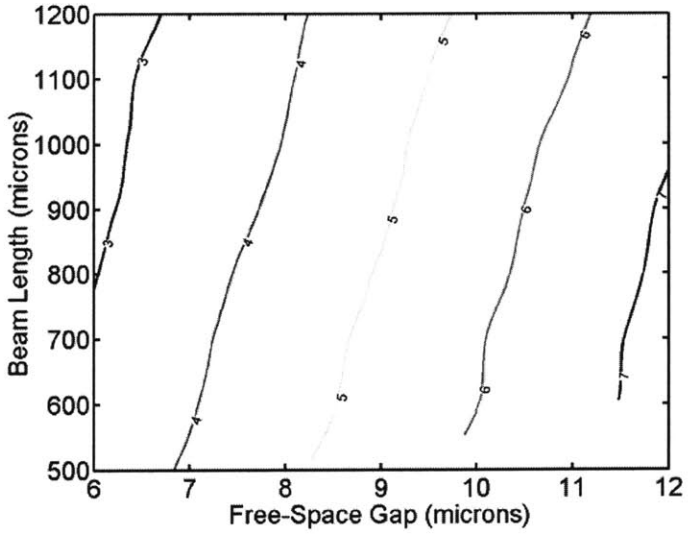

Figure 2.8: Contour plot showing effects of free-space gap (g_1) and beam segment length (L) on the maximum travel of a 1 micron thick doubly supported beam with 15 MPa of tensile stress.

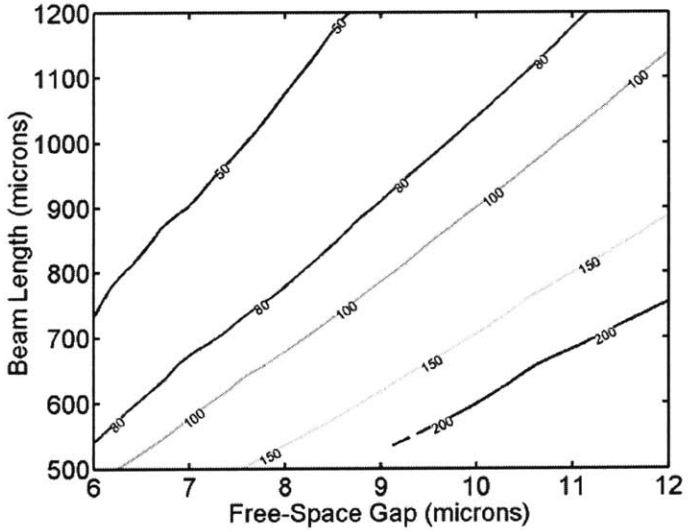

Figure 2.9: Contour plot showing effects of free-space gap (g_1) and beam segment length (L) on the pull-in voltage of a 1 micron thick doubly supported beam with 15 MPa of tensile stress.

It is desired to have devices that can be displaced by 6 microns under 130 Volts (see hatched area in Figure 2.10). The enabling free-space gap for these conditions is between 11 and 12 microns. Since processing had not been performed for these thick sacrificial layers in previous Polychromator designs, a range of thicknesses were chosen in the initial fabrication run, targeting between 3 and 5 microns of vertical displacement. In order to fabricate operating devices for each of these gaps while using only one mask

set, beam lengths on the mask set were chosen to span the design space. This allows a variety of device configurations to be fabricated while experimentally exploring the design space. Figure 2.11 shows the variation in voltage-displacement characteristics for designs of varying beam length with a fixed gap. This shows the effects observed on the contour plot of decreasing travel and actuation voltage with increasing beam length.

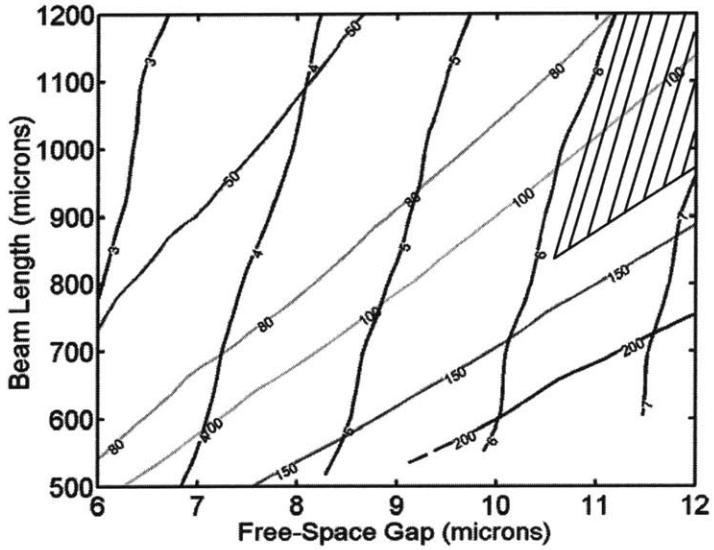

Figure 2.10: Contour plot showing effects of free-space gap (g_1) and beam segment length (L) on the maximum travel and pull-in voltage of a 1 micron thick doubly supported beam with 15 MPa of tensile stress.

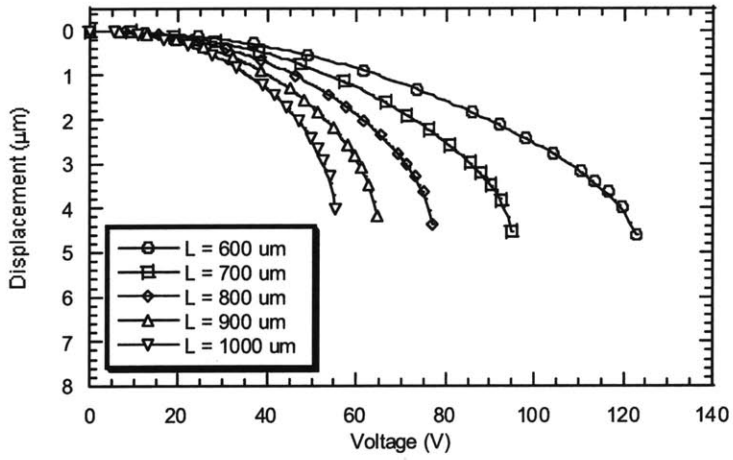

Figure 2.11: FDM simulation of varying beam lengths for an 8 micron lower gap and a 1 micron lower beam thickness with 15 MPa stress. Only the free travel of the grating element before contact is shown.

2.2.3 Effects of Stress

Once a device has been fabricated, residual beam stress is one of the most significant determining factors affecting device performance. To understand the robustness of a design, it is important to know how stress affects the transfer characteristic between applied voltage and resulting displacement; fabrication tolerances should include the range of stresses for the design to operate according to specifications. In this illustration, the lower beam segment length L = 600 μm, the lower beam thickness t_1 = 1 μm, the lower gap thickness g_1 = 8 μm (as defined in Figure 2.1 and Figure 2.2). The Young's modulus E = 160 GPa, and the beam and electrode width w = 20 μm. Figure 2.12 shows that as the stress increases from 0 to 30 MPa tensile, the actuation voltage for a given displacement increases by 40%, and the maximum displacement decreases by 25%. Methods for controlling stress are discussed in the following chapter.

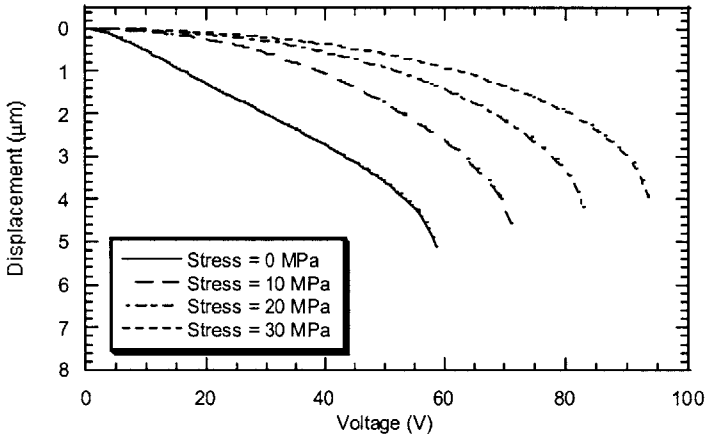

Figure 2.12: FDM simulated voltage displacement transfer functions for varying stress for an 8 micron lower gap and a 1 micron lower beam thickness.

2.2.4 MEMCAD Analysis

The MEMCAD software [43] is used to simulate the behavior of the two-level beam structure in a coupled electromechanical simulation. This simulation models the bending of the lower beam, the contact of the upper beam with the post of the lower beam, and the bending of the upper beam. Using MEMCAD, it is possible to find the pull-in voltage of the lower beam alone and the pull-in voltage of the spring-stiffened two-beam structure. This simulation provides a very accurate analysis of the behavior, but requires significantly more computation then FDM analysis.

The MEMCAD model of the beam is constructed by creating a two dimensional layout of the beam (defining the beam segment length L = 600 μm (Figure 2.2), and the beam and electrode width w = 20 μm) and then describing the process flow (defining the lower beam thickness t_1 = 1 μm, the upper beam thickness t_2 = 2.5 μm, the lower gap thickness g_1 = 8 μm, and the upper gap thickness g_2 = 4 μm, shown in Figure 2.1), which

extrudes the two-dimensional layout into a three-dimensional structural model. The material properties of each polysilicon layer (the Young's modulus E = 160 GPa, and the residual stress σ_0 = 20 MPa) are then entered into the simulation. Mechanical boundary conditions are applied such that the electrode and base of the lower beam are fixed. The two-tiered beam segment is fixed in the y-plane (perpendicular to the direction of the beams) at the ends of the upper and lower beams. These are symmetrical conditions such that when segments are connected together (end to end) the model describes the combined behavior of the connected segments. Electrical boundary conditions are applied such that the beams are electrically grounded, and the electrode is set to the applied voltage. The design of the two-beam structure with no applied voltage is shown in Figure 2.13a. Once voltage is applied to the lower electrode, the lower beam bends (Figure 2.13b) under the attractive force created by opposite charges accumulating on the beam and the electrode. As the voltage is increased, the beam continues to bend until the mirror beam contacts the lower beam support posts (Figure 2.14a). This is the point of maximum travel in the operating region of the device, within which the mirror beam remains flat. As the voltage is increased, the lower beam continues to bend, and the mirror beam starts to bend (Figure 2.14b), increasing the effective stiffness of the lower beam. This increases the stability of the device and is the main feature of the multi-layer nonlinear spring design. This effect is shown in a plot of the displacement of the mirror beam, at the location of the mirror beam support, versus applied voltage (Figure 2.15). Stepping through voltages and measuring the maximum resulting displacement from the simulation provided the data points for this plot.

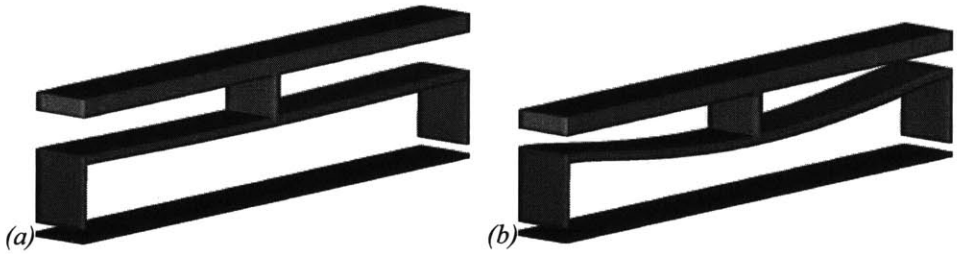

Figure 2.13: Ideal two-beam structure in MEMCAD (a). Two-beam structure under partial actuation, lower beam bends upper beam remains flat (b).

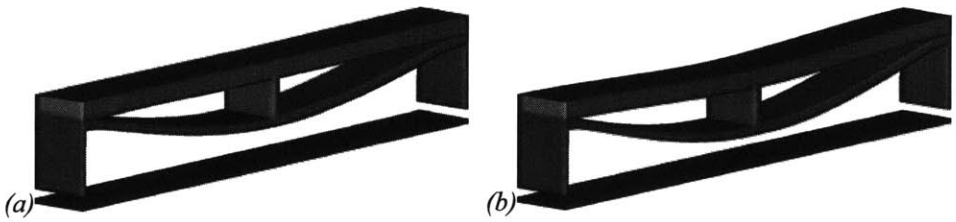

Figure 2.14: (a) Upper beam makes contact with posts of lower beam at maximum travel in operating region. (b)Upper beam bends upon further actuation stiffening the lower beam and providing a safety margin before pull-in.

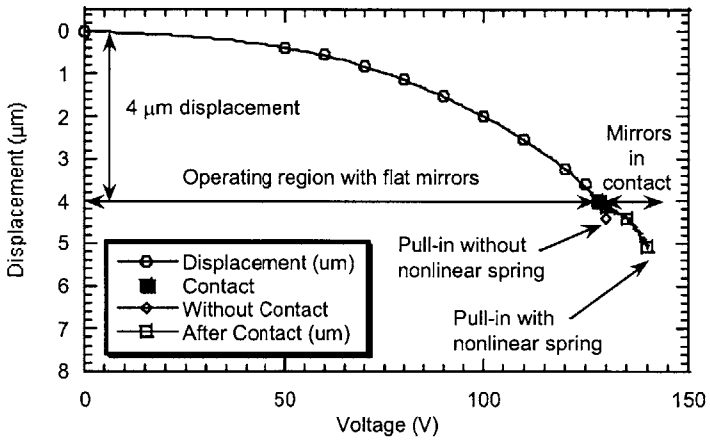

Figure 2.15: Plot of displacement versus voltage for the multi-layer nonlinear spring design. Data was obtained from coupled electromechanical MEMCAD simulations.

2.2.5 Comparison of Modeling Techniques

To quantify the differences between the simulation tools, the three modeling techniques used are compared in this section, using an ideal doubly clamped beam. For this analysis, the beam segment length L = 600 μm, the beam thickness t_1 = 1 μm, the gap thickness g_1 = 8 μm, the Young's modulus E = 160 GPa, the residual stress σ_0 = 15 MPa, and the beam and electrode width w = 20 μm. The energy method simulation provides only an estimate of the voltage-displacement transfer function, but (as shown in Figure 2.16) it does capture the basic shape of the voltage-displacement curve. Energy method analysis estimates the pull-in voltage 5% lower and the displacement, at the pull-in voltage, 10% lower then the other models, but provides insight into the analytical functions that describe the design. The FDM simulations are specific to an ideal beam with fixed boundary conditions. The simulation is slower then the energy method but still allows all parameters in the design space to be varied without significant computation. As shown in Figure 2.16 the FDM simulation differs from the MEMCAD simulation by approximately one percent, making it a very adequate and useful method for the exploration of a large design space with many variables. The MEMCAD model is comprised of a three-dimensional fixed electrode directly below a beam rigidly supported at both ends. MEMCAD performs coupled electromechanical simulations of the attractive force caused by an applied voltage on the electrode and the mechanical restoring force in the bending beam. The benefit of the MEMCAD software is that it can handle exact structural geometry and non-ideal boundary conditions, making the results significantly more consistent with actual device behavior.

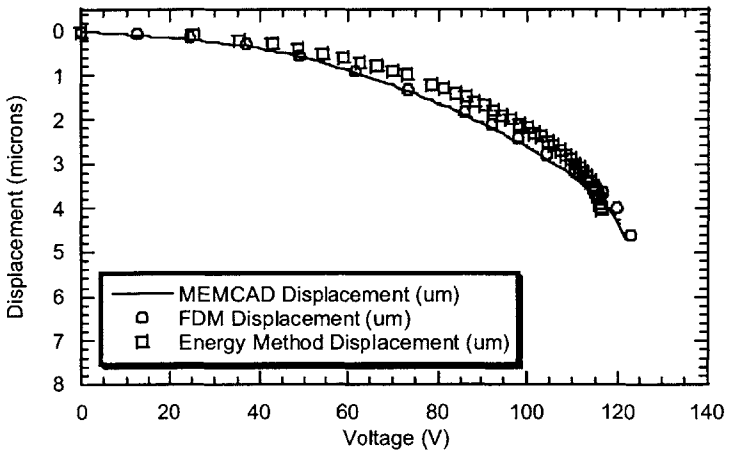

Figure 2.16: Comparison of the three modeling techniques in this chapter.

2.3 Design Challenges

The use of thinner beams creates a number of stress control hazards, because tensile stress in one layer can induce buckling in a lower layer, and conformal supports can significantly affect the device operation. Paying close attention to the end effects of the centimeter long grating element and to supports and their compliance has solved these issues.

2.3.1 Grating End Effects

A curling effect in the upper mirror beam, located at the end of the grating elements, was observed in the near-infrared Polychromator, and was found to cause premature device failure upon operation (Figure 2.17). Devices exhibiting this undesirable end effect reached pull-in at a lower voltage than ideal modeling suggested and did not travel as far. After observing this effect experimentally, modeling of the end of the grating element was performed and the simulation results matched the experimentally observed phenomena with 20 MPa residual tensile stress in the polysilicon layers (Figure 2.18).

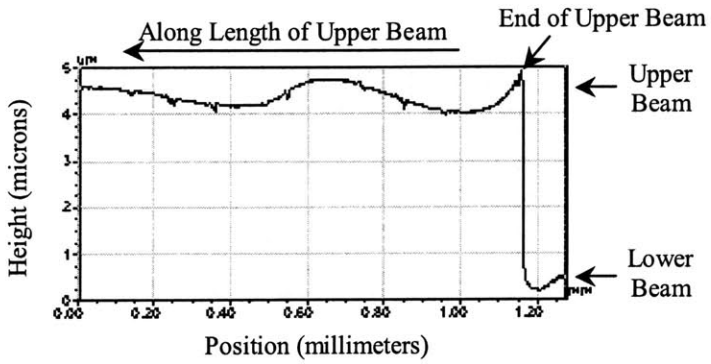

Figure 2.17: Two-dimensional profile of the end of a grating element showing the deformed upper surface.

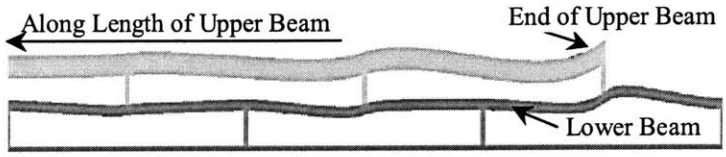

Figure 2.18: MEMCAD modeling of last three pixels showing deformed upper beam due to 20 MPa tensile stress in both beam layers.

In the center of the grating the pixels are essentially symmetric, and at the end of the grating the pixels are not symmetric. Tensile stress in the upper mirror element causes the element to shrink towards the center of the grating element because it is not rigidly attached at its ends. For the last few pixels, the lateral displacement of the mirror beam pulls the lower beam, to which it is attached, towards the midpoint of the grating element. This non-uniform behavior can be observed with an optical surface profilometer (Figure 2.17) and in simulation (Figure 2.18).

Under a uniform load applied to the lower beams (to simulate electrostatic actuation) the right pixel shows part of the lower beam displaced closer to the substrate than it would be in other parts of the mirror beam; this causes pull-in to occur at that location (Figure 2.19). Pull-in at this location would result in a lower pull-in voltage and a set of beams with decreased maximum stable travel.

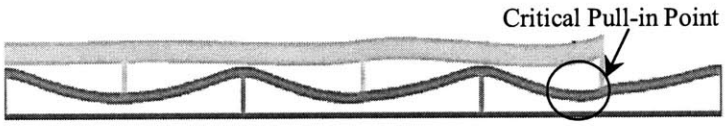

Figure 2.19: MEMCAD modeling of last three pixels under a uniform load. The lower beam in the right pixel is displaced asymmetrically, causing pull-in to occur before it would if the beam were symmetric.

To eliminate this end effect, the mirror beam is extended on the rightmost pixel to connect to a fixed support at the edge of the grating; this balances the tensile stress in the upper beam (Figure 2.20). Upon application of a uniform load to the lower beams in the

modified design, the mirror beam bends at the end of the grating element but becomes flat after two to three pixels (Figure 2.21). The lower beams, at the end of the grating element, bend but do not travel as far as the beams in the center of the mirror beam due to the increased effective stiffness of the beams caused by the addition of the tethers. Regardless of whether the added tethers are as wide as the whole beam, or only a portion of the full width, the resulting simulated structure does not exhibit the premature pull-in end effect. If the tethers are not the full width, the mirror beam will become effectively flat in a shorter distance, but some surface deformation can be observed at the ends of the grating element. The improved design was fabricated in the mid-infrared Polychromator and the previously observed end effect was eliminated.

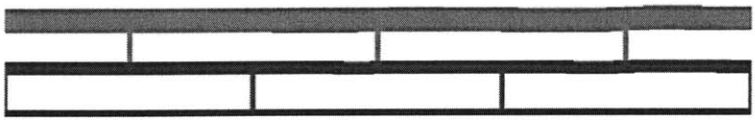

Figure 2.20: MEMCAD modeling of last three pixels where upper beam is extended on right pixel to connect to a fixed support at the edge of the grating.

Figure 2.21: MEMCAD modeling of last three pixels showing effect of upper beam extension under a uniform load. Premature pull-in is averted at the expense of non-flat upper beam for 2-3 pixels.

2.3.2 Support Compliance

The voltage-deflection characteristic of a beam is strongly dependent on the beam's support structure. Ideal supports have fixed boundary conditions on both ends of the beam (Figure 2.22a). Planar supports have fixed boundary conditions at the base of the support and have a planar upper surface (Figure 2.22b). Conformal supports have the same fixed boundary as the planar support but the thickness is constant because the material covers the underlying topography (Figure 2.22c). Conformal surface micromachining creates stepped-up supports as shown in Figure 2.22c that are structurally weaker, and have lower overall stiffness, than an ideal support with rigid boundary conditions. This results in a lower pull-in voltage and decreased maximum vertical travel. As the polysilicon thickness decreases and the sacrificial oxide thickness increases, the support becomes even weaker, further reducing maximum displacement. Due to the tiled nature of the structure, however, the support can be made more rigid by balancing the tension on both sides of the support by having the film be continuous and planar for part of the support width (Figure 2.23b and Figure 2.24) as compared to (Figure 2.23a).

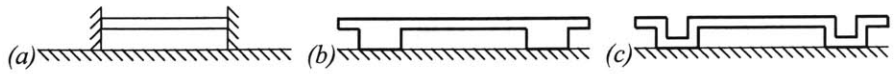

Figure 2.22: (a) Ideal Supports (b) Planar Supports (c) Conformal Supports

MEMCAD modeling of various support types shows this effect. The models in Figure 2.23 and Figure 2.24 show three support regions and the beam and electrode connected to both sides of the center support. Simulation of a simple conformal model of the support structure is shown in Figure 2.23a. Another model of the support shows a conformal ring around a large post (Figure 2.23b) that is significantly more robust than the simple conformal support, due to the stress balance from one beam segment to the next on the lower beam. Taking this concept further, several rectangular pillars instead of one square post can be used to attach the beam to the underlying structure, which further improves the stress balance due to the increase in beam width, at the beam support (Figure 2.24a) [36]. To maximize this effect, the beam should be continuous across its width at the support location and the supports themselves are located on either side of the beam, between grating elements (Figure 2.24b). Although this improves the stress balancing at the beam layer, there are fewer physical connections to the underlying layer making each support more critical, which could make the design slightly weaker as built then the multiple pillar design. This slight decrease in structural rigidity is a design and engineering tradeoff for significant process simplicity and improvement. The design with multiple pillars under the support is referred to as the stacked support design; the design with pillars between the grating elements, the lateral support design.

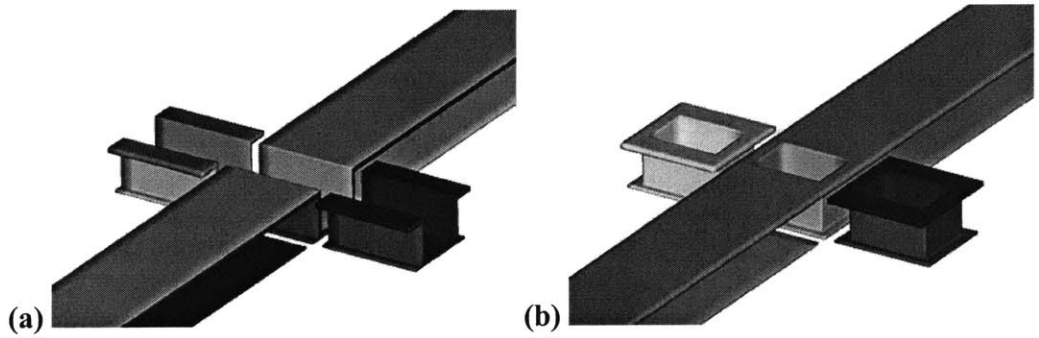

Figure 2.23: MEMCAD model of (a) conformal step-up support and (b) conformal ring support design.

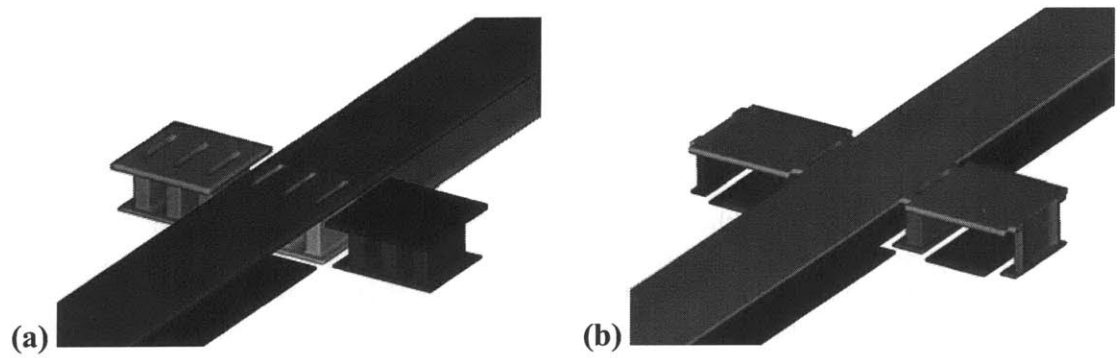

Figure 2.24: MEMCAD models of (a) stacked support design where the support consists of small pillars and (b) lateral support design where the support consists of pillars in between the beams with nothing above the electrode.

The relative stiffness of the four support structures shown in Figure 2.23 and Figure 2.24 are compared to an ideal doubly clamped beam segment in Table 2.1. The models use a beam segment length of 608 μm, a beam thickness of 1 μm, a gap thickness of 8 μm. The Young's modulus is 160 GPa, the residual stress is 15 MPa, and the beam and electrode width are 20 μm. Three identical segments are tiled together at their ends to eliminate end effects caused by boundary conditions, and a uniform 500 Pascal load is applied to the entire three beams and the resulting deflection of the midpoint of the center beam is calculated. It is evident from these simulations that the stress balancing between segments at the beam layer is critical to ensuring a rigid support.

Support Type	Beam Displacement	Reference
Conformal Step-Up	7.15 μm	Figure 2.23a
Conformal Ring	1.48 μm	Figure 2.23b
Stacked Support Pillars	1.38 μm	Figure 2.24a
Lateral Support Pillars	1.36 μm	Figure 2.24b
Ideal doubly clamped	1.34 μm	Figure 2.22a

Table 2.1: Stiffness of five support structures measured by the mid-beam segment displacement of a 608 micron beam (as measured between the support connections to the lower layer or at the end of the ideal clamped beam) following application of a 500 Pascal load to the beam segment surface.

2.4 Summary

A design was presented in this chapter that made use of stress stiffening to achieve large displacement and a multi-layer nonlinear spring to prevent device failure. The design was simulated using energy method analysis, finite difference method simulations, and the commercial MEMCAD software. Design challenges were overcome by analysis and simulation of previously observed phenomena. The electromechanical design was robust in simulation and the fabrication sequence for realizing the device is presented in the following chapter.

Chapter 3: Fabrication

This chapter describes the fabrication sequences and process development used to build the Polychromator. The fabrication process for the Polychromator was designed and developed in collaboration with Dr. Dan Youngner at Honeywell Laboratories. The process incorporates the fabrication insights from the previous Polychromator processes and adapts them to the new requirement of large actuation. The majority of the processing is performed at Honeywell Laboratories; this includes the deposition and etches of oxide, polysilicon, and metal, the photolithography, and the dice and release process. Critical dielectric nitride and oxide depositions are done at MIT in the Integrated Circuit Laboratory (ICL), which is part of the Microsystems Technology Laboratory (MTL). The insulating nitride layers are deposited in a Thermco Vertical Thermal Reactor (VTR). The sacrificial silicon dioxide layers are deposited in a Novellus Concept-One plasma enhanced chemical vapor deposition (PECVD) system.

One of the key technological advances in this work was a method for depositing the thick oxide layers needed in the mid-infrared design. The team at Honeywell also made processing advances in the control of stress in the films and on the wafer, the release process for the devices, and the packaging. These are also described briefly here. Two different structural designs are described; the stacked support design (Section 3.1.1) was fabricated, but process tool limitations prevented successful completion of a critical etch and thus successful completion of the device fabrication. The lateral support design (Section 3.1.2) simplified the fabrication process, reduced the number of layers needed, and included a new support structure designed to be robust against the lack of selectivity of the etching tools. This modification demonstrates the relationship between design and fabrication: a process limitation dictated a new design choice for the support. The final section of the chapter shows pictorially the results of fabrication.

3.1 Fabrication Process

The fabrication processes for the stacked support design and the lateral support design are described in this section. Cross-sectional pictures describe the process flow, illustrating the combination of the masks and the process steps used to create the device. Cross sections are shown using two pictures: the left is a side view of two beam segments, and the right is an end-on view of several segments at the location of the lower support post. The legend for the different layers is shown in Figure 3.1 and Figure 3.13. Appendix A contains detailed descriptions of the mask layout and mask layers; Appendix B contains detailed process flows for the stacked support design and the lateral support design.

3.1.1 Stacked Support Process

The stacked support structure requires three polysilicon layers. The first is used for interconnects and electrodes, and the second two are used for the active structure. To insulate the electrodes from the beam supports, a dielectric nitride spacer is needed under each support. To reduce the topography in the upper mirror layer the spacer and previous layers are recessed into the base silicon layer.

The recess in the silicon substrate is defined and then etched using a LAM silicon etcher (Figure 3.2). Wet thermal oxide, 2 microns thick, is grown on the wafer as the primary isolation between the interconnects and the substrate (Figure 3.3). This is followed by a deposition of 0.5 microns of low stress silicon nitride which is performed with a 7:1 or 10:1 $Si_2Cl_2H_2$ to NH_3 ratio in a VTR deposition system (Figure 3.4). The base conducting layer of polysilicon, 0.5 microns thick, is deposited at 596°C. This temperature results in an as-deposited tensile stress between 300 and 400 MPa, which is reduced during the final high temperature anneal step. The polysilicon is implanted with boron at a dose of $2 * 10^{15}$ cm^{-2} at 100 KeV. The boron is diffused through the polysilison during the final anneal step. The features desired in the first polysilicon layer are photolithographically defined in a 1.2 micron resist coating. The exposed polysilicon is then etched in a LAM etcher with a recipe optimized to produce vertical sidewalls (Figure 3.5).

Figure 3.1: Legend for the deposited layers shown in the cross-sections below.

Figure 3.2: Recess is etched in silicon to minimize topography

Figure 3.3: Insulating thermal oxide is deposited over the entire wafer.

Figure 3.4: Insulating nitride is deposited over the entire wafer as an etch stop.

Figure 3.5: The first polysilicon layer is deposited and etched to form electrodes and interconnects.

The insulating spacer consists of a two-layer stack of nitride and polysilicon. The nitride is a critical insulator between the base polysilicon layer and the active polysilicon structural layers. The polysilicon protects the nitride layer because it acts as an etch stop for further processing. The nitride is 1 micron thick, and deposited under the same conditions as the previous nitride layer. The polysilicon is 0.25 microns thick and deposited under the same conditions as the base polysilicon layer. Since the density of spacers on the front surface of the wafer is very low, the polysilicon and nitride films are removed from the backside of the wafer to balance the stress on both sides. The spacers are defined in resist and both films are etched in subsequent film specific recipes in a LAM etcher (Figure 3.6).

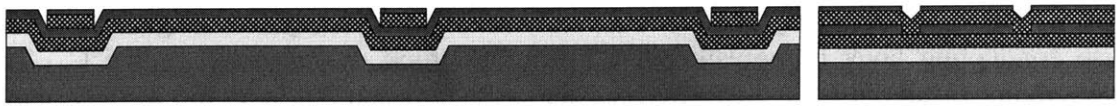

Figure 3.6: Nitride is deposited and etched to form insulating supports.

The first sacrificial layer of TEOS oxide, 6 to 12 microns thick, depending on the wafer, is deposited on both sides of the wafer in alternating deposition and anneal steps as discussed in section 3.4.1. Due to the oxide thickness and the small features required, a thick resist or a metal hardmask is needed to define the support post features to be etched in the oxide. The oxide is etched in a STS etcher with a process designed to etch oxide at a much higher rate then polysilicon (Figure 3.7). The oxide etch must produce vertical sidewalls in order to have sufficient area exposed at the base of the etched area for the subsequent polysilicon deposition.

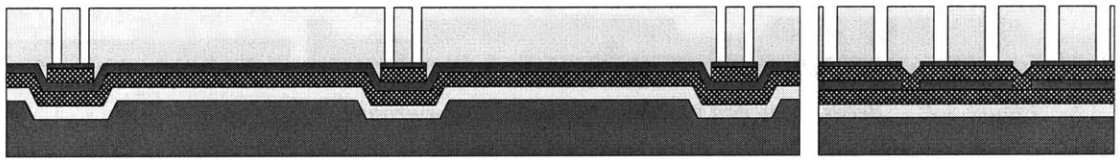

Figure 3.7: Oxide is deposited and etched to form the first actuating gap.

The first structural layer of polysilicon is 1 micron thick and is deposited under the same conditions as the base layer of polysilicon. The boron is implanted with a dose of $4 * 10^{15}$ cm^{-2} at 150 KeV. The increase of dopant intensity from the base layer is needed because the boron must be diffused through the thicker structural layer. The polysilicon is then patterned and etched to form the lower bending beams of the device (Figure 3.8). Making the features in the previous thick oxide small and depositing a thickness of polysilicon comparable to the feature size minimizes surface topography.

The second sacrificial layer of TEOS oxide is 3 to 6 microns thick. For thinner layers, the oxide is deposited on both sides of the wafer in one step, followed by an anneal; for thicker layers, the oxide is deposited in alternating deposit and anneal steps. The structural connections between the two active layers of polysilicon are patterned and etched into the oxide using a similar etch to that used for the previous sacrificial oxide (Figure 3.9). The second structural polysilicon layer, 2 to 3 microns thick, is deposited and implanted under the same conditions as the first structural polysilicon layer. The

implant for this thickness is not as important as the lower polysilicon layers because the layer rides on top of the lower layer and has no electrical function. The polysilicon is then patterned and etched with similar conditions to the previous polysilicon layers, to form the mirror beams of the device (Figure 3.10). After structural polysilicon fabrication is complete, the device is annealed for several hours at 950°C to drive in the boron dopants and to reduce the residual polysilicon stress to an acceptable tensile level.

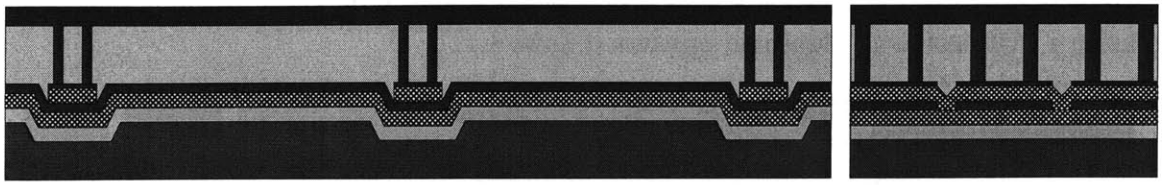

Figure 3.8: The second polysilicon layer is deposited and etched to form the first actuating beam. The fill of the previous oxide etch creates the supports for this layer.

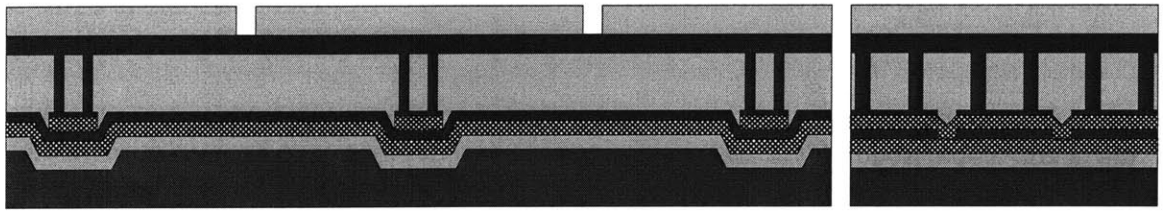

Figure 3.9: Oxide is deposited and etched to form the second actuating gap.

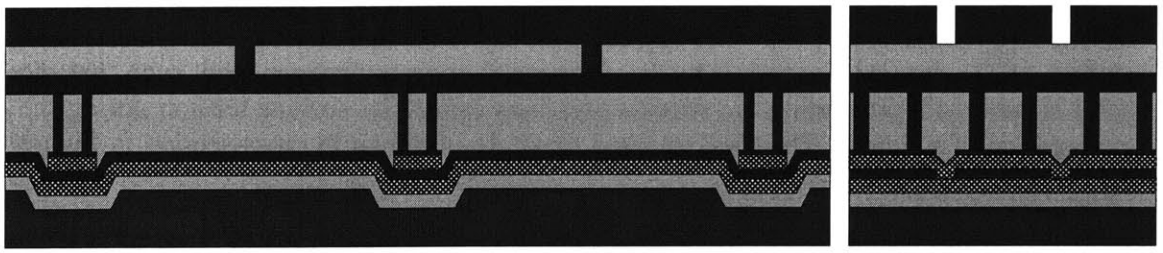

Figure 3.10: The third polysilicon layer is deposited and etched to form the second actuating or mirror beam. The fill of the previous oxide etch again creates the supports.

During the sacrificial release, all the oxide on the front side of the wafer is removed. If the oxide remained on the back side of the wafer, the compressive residual stress would cause the wafer to curl concave up (center down and edges up). Due to the thickness of the oxide films, the large curvature can impart a significant decrease in the effective stress in the polysilicon beams on the front surface, to such an extent that the beams buckle. This necessitates the removal of the backside oxide films. The front surface of the wafer is protected with resist, while the two upper polysilicon layers are removed from the back of the wafer using two RIE etches, with a buffered-oxide-etch (BOE) between them to remove the second sacrificial oxide. The first sacrificial oxide is removed during the final release etch.

Metal is deposited and defined for bond pads in a lift-off process. The front surface of the wafer is coated with approximately 3 microns of resist. The bond pad features are etched away, and 0.5 microns of gold are deposited by e-beam evaporation. The resist is then wet etched, which causes the unwanted gold to float off the wafer. A self-aligned reverse lift-off process is used to cover the mirror beams with 50 nanometers of gold. About 0.5 microns of the exposed oxide between the beams is wet etched; the metal is then deposited, and the gold that does not adhere to the polysilicon is removed using a BOE etch with ultrasonic agitation (Figure 3.11).

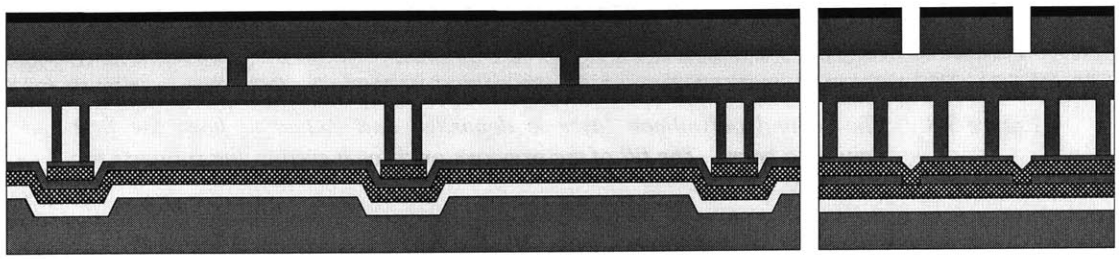

Figure 3.11: Gold is deposited and etched to form the reflective mirror surface.

To complete device fabrication, the wafers must be diced and then released at the die level. The front of the wafers are protected with resist and then each wafer is separated into individual die. The release of the beams requires wet etching the exposed sacrificial oxide on both sides of the wafer. To prevent stiction following the wet release etch and to prevent in-use stiction, the die undergo a supercritical dry as described by Legtenberg [46] and are then coated with a self-assembled monolayer (SAM) as described by Srinivasan [47]. The supercritical dry process freezes cyclohexane on the surface of the die and the temperature is decreased under a nitrogen flow such that the solid is sublimed, preventing the stiction problems caused by surface tension during the evaporation of a liquid. The final released structure is shown in cross-section in Figure 3.12.

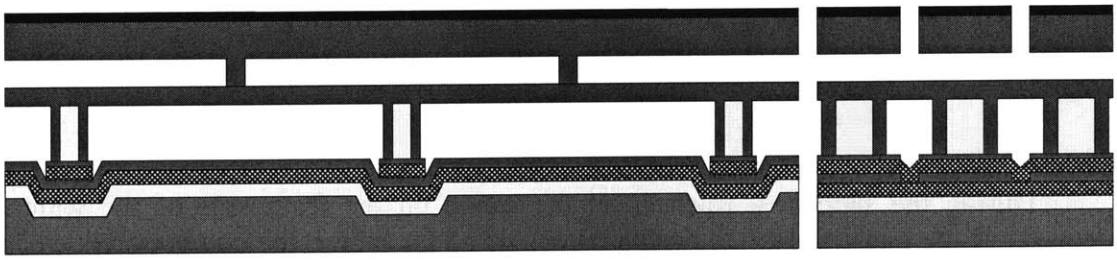

Figure 3.12: The sacrificial oxide is removed to release the beams.

3.1.2 Lateral Support Process

The lateral support structure differs from the stacked support structure in the details of the support post for the lower bending beam. Instead of placing large supports directly under each beam to connect each beam to the lower surface, the lower beams of

adjacent grating elements are connected together by the shared support; the support post for adjacent beams is located in the space between the beams. The electrode then passes directly under the support structure between posts and is made slightly narrower to accommodate the support posts on either side of it. This design eliminates the need for an insulating spacer and thus the need for the silicon recess. The complexity of the process is therefore reduced; the process is shorter by two deposition steps, two photolithography steps, and the critical etch to form the lower support. Although lateral supports are slightly more compliant then stacked supports, the process simplification enabled the successful fabrication of the device.

The processing for the lateral support design does not require the silicon recess so the topography for the lower layers is greatly reduced. Wet thermal oxide, 1 micron thick, is grown on the bare silicon wafers (Figure 3.14). This is followed by 0.5 microns of low stress silicon nitride to complete substrate isolation (Figure 3.15). The base layer of polysilicon, 1.0 micron thick, is deposited, implanted, patterned, and etched similarly to the previous process to form interconnects and electrodes (Figure 3.16).

Figure 3.13: Legend for the deposited layers shown in the cross-sections below.

Figure 3.14: Insulating thermal oxide is deposited over the entire wafer.

Figure 3.15: Insulating nitride is deposited over the entire wafer as an etch stop.

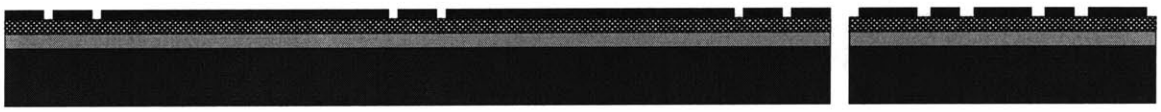

Figure 3.16: The first polysilicon layer is deposited and etched to form electrodes and interconnects.

The first sacrificial layer of TEOS oxide, 6 to 12 microns thick, is deposited on both sides of the wafer in alternating depositions and anneals. The oxide is etched in a STS etcher with a similar etch as used in the previous process. This process is more robust, however, because an overetch does not harm the device (Figure 3.17). The first structural layer of polysilicon, 1 micron thick, is deposited, doped, defined, and etched under the same conditions as in the previous design (Figure 3.18).

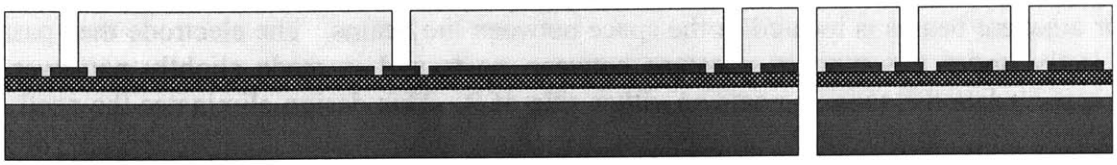

Figure 3.17: Oxide is deposited and etched to form the first actuating gap.

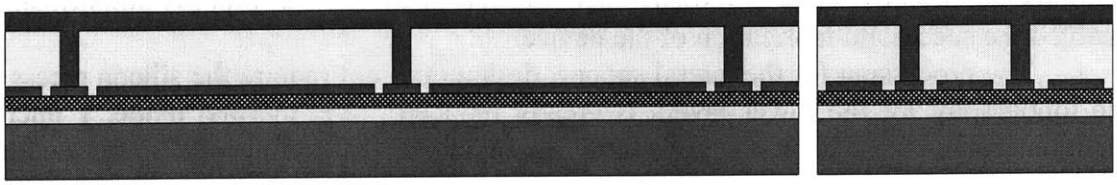

Figure 3.18: The second polysilicon layer is deposited and etched to form the first actuating beam. The fill of the previous oxide etch creates the supports for this layer.

The second sacrificial layer of TEOS oxide, 3 to 6 microns thick, is deposited on both sides of the wafer under similar conditions as in the previous process. The upper posts between the bending and mirror beams are patterned and etched into the oxide using a similar etch to the previous sacrificial oxide (Figure 3.19). The second structural polysilicon layer, 2 to 3 microns thick, is deposited, implanted, patterned, and etched similarly to the previous process to form the mirror beams of the device (Figure 3.20). With the completion of the structural polysilicon fabrication the device is annealed for several hours at 950°C to drive in the boron dopants and to reduce the residual polysilicon stress to an acceptable tensile level.

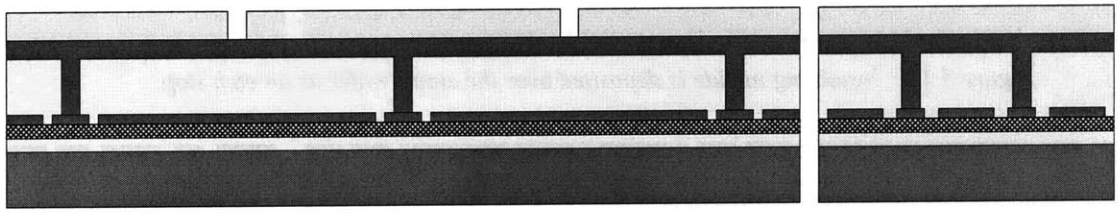

Figure 3.19: Oxide is deposited and etched to form the second actuating gap.

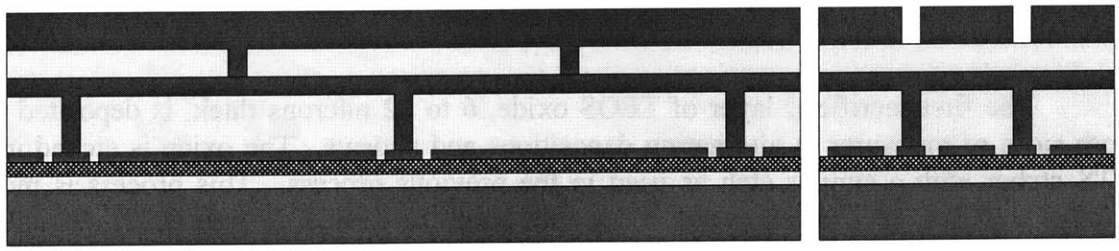

Figure 3.20: The third polysilicon layer is deposited and etched to form the second actuating or mirror beam. The fill of the previous oxide etch again creates the supports.

Metal is deposited and defined for bond pads in a lift-off process similar to that used for the previous design. An alternate metalization, dice, and release method was used since the gold-polysilicon interface was attacked during the release etch. Following bond pad metalization, the wafers are diced and released before mirror metal deposition. The wafers are supercritical-dried, SAM coated, and then supercritical-dried again. A shadow mask is used to deposit metal on the active portion of the structure at +60 and -60 degree angles to the normal, perpendicular to the orientation of the grating elements. This covers the top and parts of the sides of the beams. Since the beams are closer together than they are thick, no gold penetrates to the lower structure between the beams. This method results in superior reflective mirror surfaces because the gold surface and the gold-polysilicon interface are not attacked during the release etch. The resulting structure shows the difference between the designs, namely the supports and the topography (Figure 3.21).

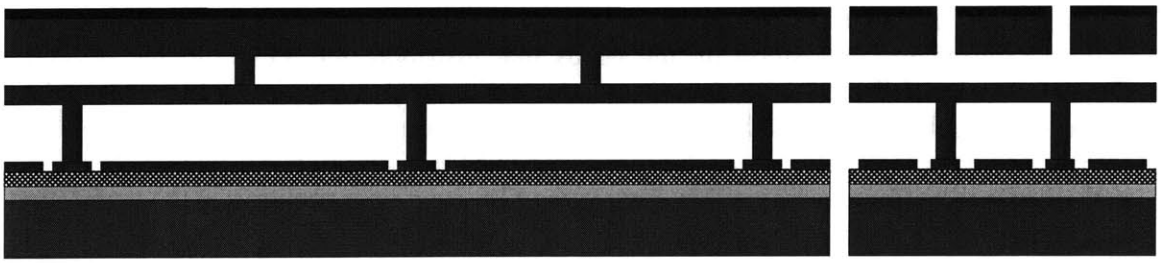

Figure 3.21: The sacrificial oxide has been removed and the gold mirror layer has been deposited.

3.2 Process Development

To successfully fabricate the Polychromator devices, several processing challenges had to be addressed. This section describes work done both at MIT and at Honeywell. Specifically, the thick oxide process was developed at MIT as a critical part of this thesis, and subsequently transferred to Honeywell. Achieving the desired large displacement required the deposition and etching of thick sacrificial layers; both types of steps had numerous and significant difficulties. The control of the polysilicon residual stress was another key fabrication challenge because performance is so strongly dependent on stress. The combination of polysilicon and oxide stress caused problems including wafer curvature and wafer shrinkage. Post-processing of the wafer, including gold metalization and release continually posed processing difficulties. The final step in building the Polychromator was the packaging of the 512-channel device for prototype electrical and optical testing. Addressing the problems in each of the aspects of fabrication required several iterations between design and fabrication.

3.2.1 Thick Oxide Layers

The Novellus Concept-One [48] PECVD system is capable of depositing many films including nitride, oxynitride, silane-based oxide, and tetra-ethel-ortho-silicate (TEOS) based oxide. TEOS was chosen over other oxides because deposited TEOS exhibits high conformality, uniformity, low stress, and its capability for thick film deposition. Good conformality is a result of the low deposition temperature of 350°C and the liquid based source. Cycling each wafer through five deposition stations enables good uniformity by averaging non-uniformities created by any one of the five stations. Low as-deposited stress is a result of the PECVD process. When the film is annealed at or above 850°C it outgases and takes on the stress and properties of oxide. Very thick film depositions have been demonstrated by Ghodssi et. al. [49].

There are several problems associated with depositing thick oxides in the Concept-One, however. If films thicker than 4 to 5 microns are deposited, flakes can build up during the deposition on the heads that distribute the TEOS to the plasma. These flakes can fall off the heads and onto the wafer; they can typically be removed by cleans or a touch CMP, but still contribute to the defects on the wafer. Another problem associated with a thick film is that the film stress of a thick film imparts much more stress to the wafer than film stress in a thin film. If the film is on only one side of the wafer, the film stress can cause significant wafer curvature, making further processing difficult and also greatly affecting the resulting stress state of the wafer; this effect can potentially result in unusable die.

If a thick film is deposited on the front and back side of a wafer to equalize stress and minimize wafer curvature, the as-deposited film is very uniform but when the film is annealed cracking is observed in the oxide. In addition, backside processing in the Novellus Concept-1 chamber causes cross-contamination of particulates from the wafer handling equipment to the front side of the wafer. If the front side of the wafer were protected by another film, such as nitride, the particulates (some are oxide) would act as an etch mask when trying to remove the nitride. This problem could be overcome by an oxide etch, but then the backside would have to be protected as well; adapting this approach to thick layer deposition would have resulted in an overly complicated process so a simpler approach was implemented.

When the deposition is done in several steps, flaking is reduced or eliminated during deposition but cross contamination from the wafer handling equipment is still a problem. A robust process was developed, with few defects and no cracking, by depositing thin films on both sides and then annealing. TEOS 3-4 microns thick was deposited on the backside of the wafer. The wafer was then cleaned, and exposed to a 30 second 50:1 Hydrofluoric Acid (HF) to de-ionized (DI) water etch to free up the oxide particles. TEOS of the same thickness was then deposited on the front of the wafer, and the wafer was then annealed at 850°C to allow it to outgas. The previous steps were repeated until the desired film thickness was achieved. Films up to 12 microns were deposited using this technique without cracking or curvature.

Once a thick sacrificial oxide film is deposited, it must be defined, etched with vertical sidewalls, and the etch must have the selectivity to stop on a layer such as polysilicon. The sidewall profile and the etch selectivity and is heavily dependent on the available process technology. In this process an STS etcher was used, because it has the

ability to etch high aspect ratio features in oxide and silicon. By modifying the gas flow, it is possible to etch features in the oxide and have reasonable selectivity to silicon or nitride. The particular machine used was not able to achieve this aspect ratio without overetching into the film beneath. This caused significant problems etching the posts for the stacked support design, which relies on a polysilicon etch stop on top of a critical nitride dielectric. Devices fabricated using the stacked support design did not work and this over-etching was one likely explanation.

The lateral support design eliminated the critical dielectric; the posts, located between the grating elements, are placed such that even a significant over-etch of the oxide does not cause any electrical or structural problems. This second design enabled successful fabrication given the available process tools. Had another tool, with the ability to etch thick oxide layers with high selectivity to polysilicon, been available, this etch would not have been the limiting factor in the fabrication of the stacked support design.

Even with the more robust lateral support design, etching a 2 micron feature in 8-12 microns of oxide is a challenge and requires careful attention to the gas flow characteristics, which can adversely effect the features (Figure 3.22a) and the angle (Figure 3.22b) in an etch. Care must also be made in implementing the etch hard-mask since it can cause micro masking or "grass" to be formed during the etch (Figure 3.23a). With the correct hard-mask and gas flow characteristics, however, it is possible to etch straight sidewalls in 8-12 microns of oxide, creating a robust support (Figure 3.23b).

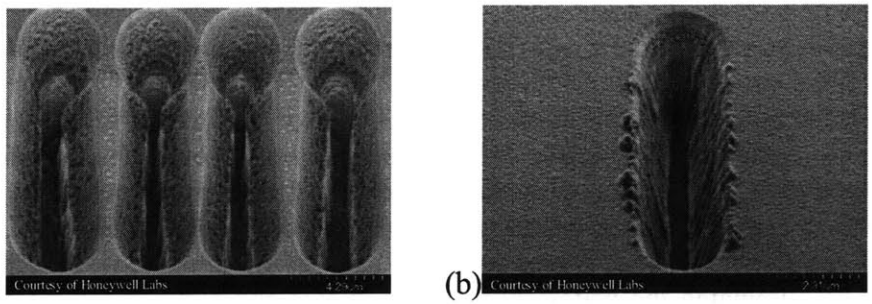

Figure 3.22: Inadequate feature definition caused by poor etch chemistry.

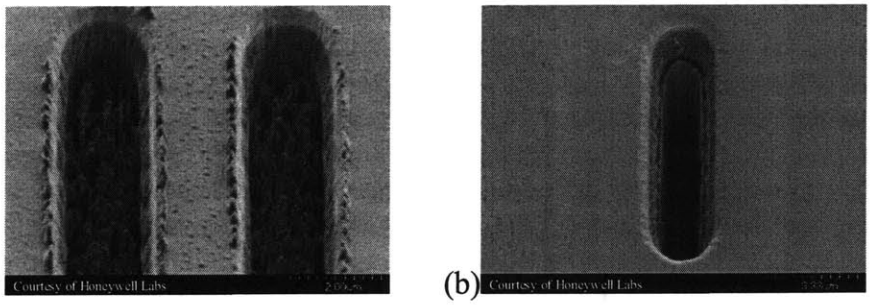

Figure 3.23: (a) Micro masking during the oxide etch. (b) straight side wall etch.

3.2.2 Stress Control

The stress in the polysilicon is one of the least controllable parameters in the fabrication process and also is the parameter that has the most significant impact on device performance, in terms of actuation voltage and achievable displacement. If the residual stress in the thin long beams is compressive, the beams will buckle and not function correctly. If the stress is too tensile, the maximum stable travel will decrease, and the actuation voltage for a given displacement will increase (Figure 2.12). The desired residual stress is therefore low and tensile; this level of stress maximizes displacement at moderate actuation voltage.

The final residual stress in the released polysilicon film is a function of the as-deposited stress, the post-anneal stress, and the wafer curvature. The as-deposited stress is a function of the deposition system, the gas flows, and the deposition temperature. The post-anneal stress is a function of the anneal time and temperature. The curvature of the wafer (caused by unmatched film stresses on either side of the wafer) imparts a post-release stress to the free beams.

The process used to fabricate the near-infrared Polychromator achieved low tensile stress post-anneal, in the range of 5 MPa, by depositing the polysilicon at 580°C and then annealing the wafers at 1100°C for 5 to 6 hours. The high temperature processing caused several deleterious effects, however, such as wafer shrinkage and wafer curvature, both of which could be caused by yielding of the silicon. The variation in the final stress in the beams was enough to make devices non-functional; some grating elements were buckled and some failed to achieve the desired travel.

The design for the mid-infrared Polychromator presented here, however, is less sensitive to stress then the design for the near-infrared Polychromator; the decreased stress sensitivity enabled the process to be modified to eliminate these damaging process steps. The polysilicon was deposited at 596°C and then annealed at 950°C for about 5 hours to reduce post-anneal stress to the 10 to 20 MPa range. The lower anneal temperature eliminated the wafer shrinkage problems and reduced the wafer curvature. The stress was targeted higher than desired to ensure tensile stress in the beams over the range of the potential variations associated with processing.

Particular attention was given to matching the thickness and stress of films on both sides of the wafer, during processing and afterwards, to reduce curvature. The only difference between the two sides of a wafer, when both have a film deposited, is that the front is patterned. Removal of a significant portion of the layer on the front side can cause an imbalance in the stress state of the wafer. The vias in the oxide are very small and etching them constitutes the removal of approximately one percent of the film. The polysilicon features in the active area, on the other hand, constitute about 50 percent of the die area; most of this area is used for routing the interconnects for the 512 active elements. To eliminate the induced stress imbalance, structures are designed to increase the percentage of the film that remains on the front side of the wafer. These hundred micron square *fill-poly* blocks, with holes to release the oxide beneath, increase the density of polysilicon to about 95 percent. Additionally, reducing the topography of the polysilicon layer facilitates a chemical-mechanical polishing (CMP) planarization process applied to subsequent oxide layers. The CMP step, although not implemented, would increase the reflectivity of the mirror surface.

3.2.3 Metalization and Release

Mirror and pad metalization are critical steps that follow the completion of the polysilicon processing. The mirror metal layer must be uniform to maximize optical efficiency, and the pad metal layer must enable good electrical contact to be made to the die. The metalization, as well as the metal-polysilicon interface, however, can be attacked by the hydrofluoric (HF) etch that releases the devices. Gold is chosen as the metal layers because it is a good reflector at the wavelengths of interest and it is typically resistant to the HF etch. The interface, however, can still be attacked during the release etch. Covering the bond pads with a wax coating protected them during the release etch, but the mirror metalization continued to be attacked. To overcome this the devices were released first and metal was deposited afterwards.

The beams are freed from the sacrificial oxide beneath them by the HF etch. If the devices are cleaned and dried however beams can stick down due to surface tension in the evaporating liquid. One method for preventing this stiction is to rinse the die in isopropyl alcohol, entrain liquid on the die, and bake on a hot plate. This results in a dramatic improvement in yield, but some beams are still stuck down following the release. A very good method for eliminating release stiction is a supercritical dry. This entrains a liquid on the die following release, freezes the liquid, and then sublimes the liquid. The resulting gas does not have surface tension and so the beams do not stick down. In-use stiction, when one beam surface contacts another during operation, can be another source of device failure. The device can be made more robust against this failure by using a self-assembled monolayer (SAM) coating that reduces the adhesion between two surfaces [46]. Since the SAM coating involves several liquid process steps, another supercritical dry step was used for the final release.

3.2.4 Packaging

The Polychromator package must be mountable in an optical system, provide electrical access to 520 pads, optical access to the chip, and not impart any external stresses to the chip. The package consists of a circuit board with six 100-pin connectors that are attached by ribbon cable to a 512-channel programmable voltage source with a 0 to 150 volt range. An interposer is used to interface the bond pads on the chip to the supply voltages on the circuit board. The interposer is made of silicon and is rigidly attached to the circuit board with a single row of bond pads on each outside edge and three rows of bond pads on each edge of the die attach. The bond pads around the outside edge are wire bonded to the circuit board, and the traces on the circuit board are distributed to the external ribbon cable connectors. The die is attached to the interposer board with a flexible adhesive, and the three rows of pads on the die are wire bonded to the three rows of bond pads on the interposer (Figure 3.24). The final package with all wire bonds is shown in Figure 3.25. A metal cover with a calcium fluoride window (for optical access) is then attached to the front of the circuit board, and a metal plate with mounting holes is attached to the back. This provides a robust platform for optically and electrically testing prototype devices. In a manufacturing high volume application, or where miniaturization is important, the drive electronics could be integrated on chip if the

process technology is available, multiplexed on chip to reduce pin counts, or built as a separate chip and attached directly to the back of the Polychromator chip.

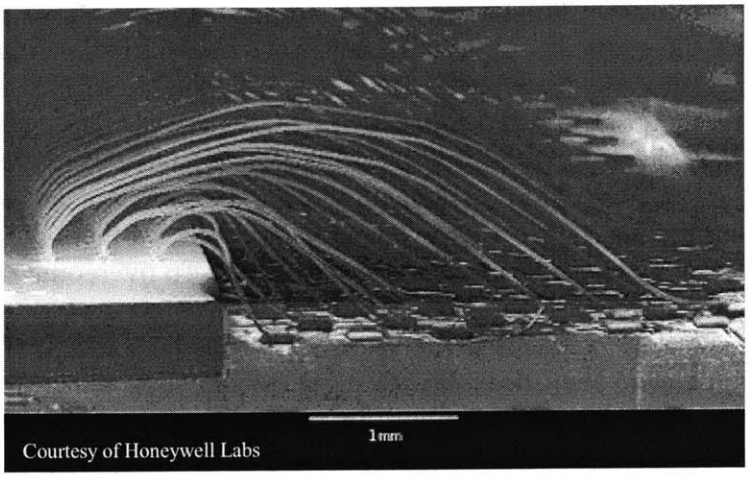

Figure 3.24: Three rows of wire bonds necessary to access all beams.

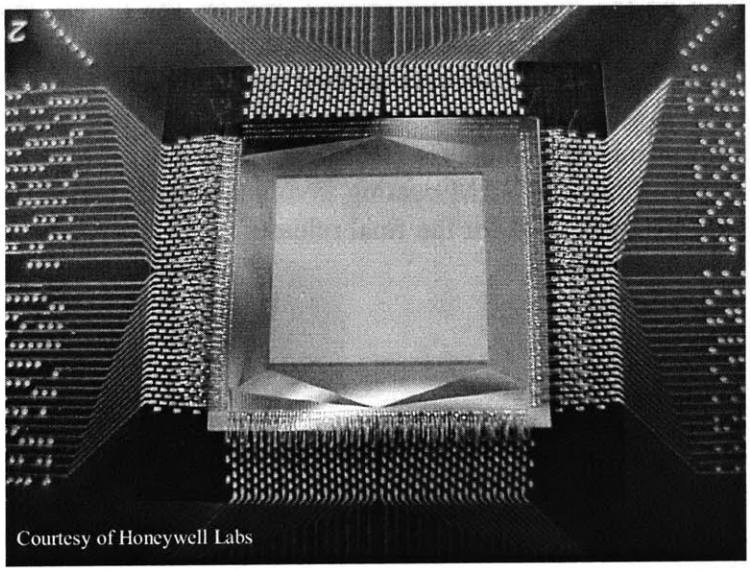

Figure 3.25: Packaged and wire bonded device.

3.3 Results of fabrication

The following section shows the results of the fabrication process through a series of scanning electron microscope (SEM) images. The features of the design and process discussed in the previous two chapters are presented. The first set of images show SEMs of the fabricated stacked support process. Figure 3.26 shows the nitride pads that have been recessed into the silicon, along with the layers beneath them. The grooves on the pads correspond to the pillars connecting the polysilicon beams (which, for illustration,

have been removed in this picture). Figure 3.27 shows the supports for the polysilicon beams. There is minimal topography in the beam surface and the support features are larger then they were designed to be because of sloped sidewalls result from the oxide etch. The devices fabricated using this process were non-functional; they suffered from dielectric breakdown due to the expanded oxide etch and the inability to stop the oxide etch on the nitride pad.

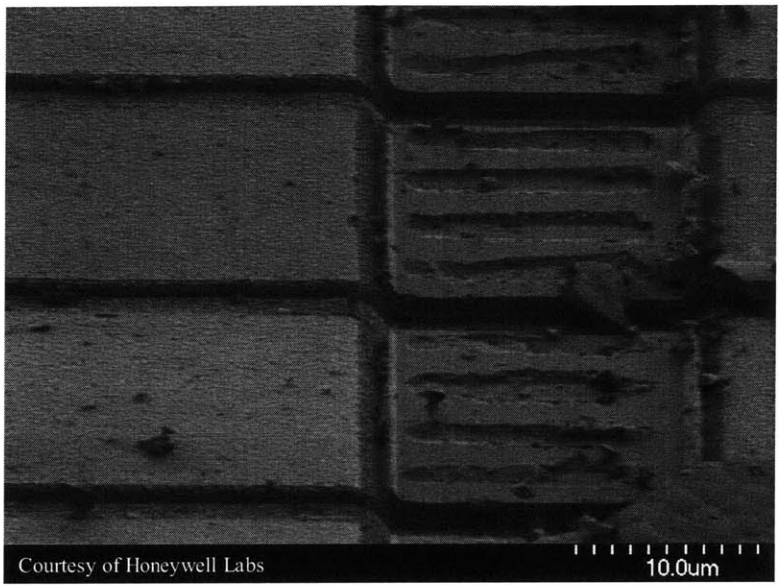

Figure 3.26: SEM showing recessed nitride pads with upper supports broken off.

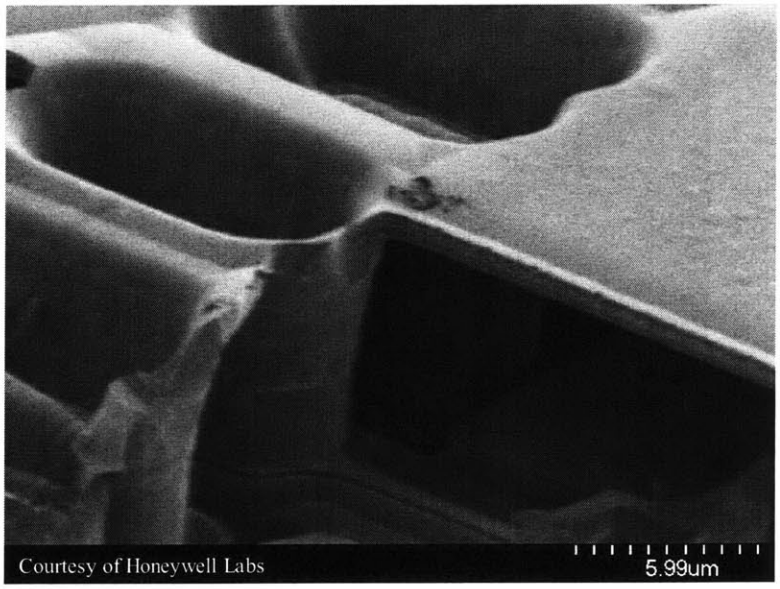

Figure 3.27: SEM showing lower beam posts and the large size of the supports due to an increased via feature resulting from the oxide etch.

The next set of images shows SEMs of the fabricated lateral support process. Figure 3.28 shows approximately 150 mirror beams, the tethers that attach the ends of the

mirror beams to a stiff support, and the fill-poly blocks that increase the density of the second poly layer. Figure 3.29 shows in more detail a side view at the edge of the active device area. The underlying electrical interconnects are evident in the topography of the fill-poly blocks, which have release holes to allow the removal of the oxide beneath. The end of the mirror beams are attached at the poly-2 support to the poly-1 layer beneath and by tethers to a solid support (shown in Figure 3.28) at the ends of the active area.

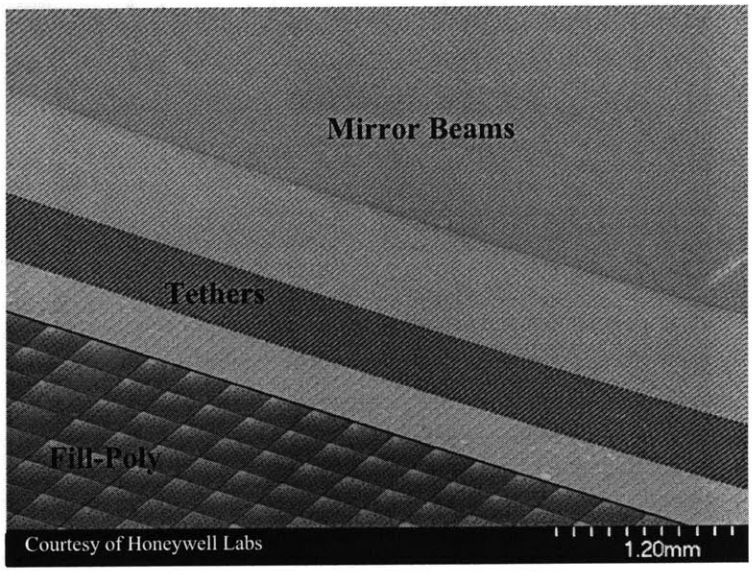

Figure 3.28: SEM of active grating area (upper right corner) with beams going in direction of upper right corner, outside fill structures (lower left), and end effect tethers (dark section going from lower right to mid left).

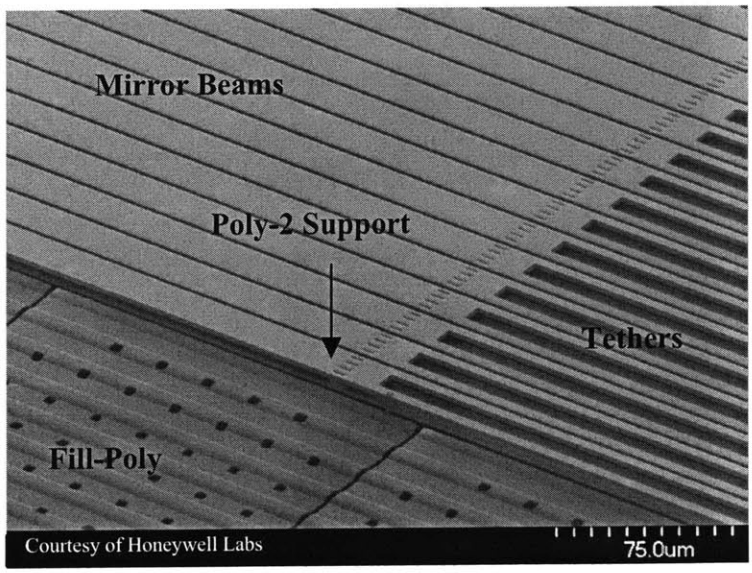

Figure 3.29: SEM of side of active grating area showing beams going in upper left direction, the poly-2 support with tethers to reduce end effects(middle to upper right), and the fill poly in the lower left corner.

Figure 3.30 shows, in more detail, the side of the active area; the fill poly has been removed, the interconnects and electrodes are visible in poly-0, the lower bending beam is visible at the same level as the fill-poly, and the features of the poly-2 support and the mirror beams are more visible. Figure 3.31 shows a close-up of the poly-2 support and the tethers, and illustrates the polysilicon surface roughness, the fill of the support posts by the polysilicon, and the sidewall roughness of the etch.

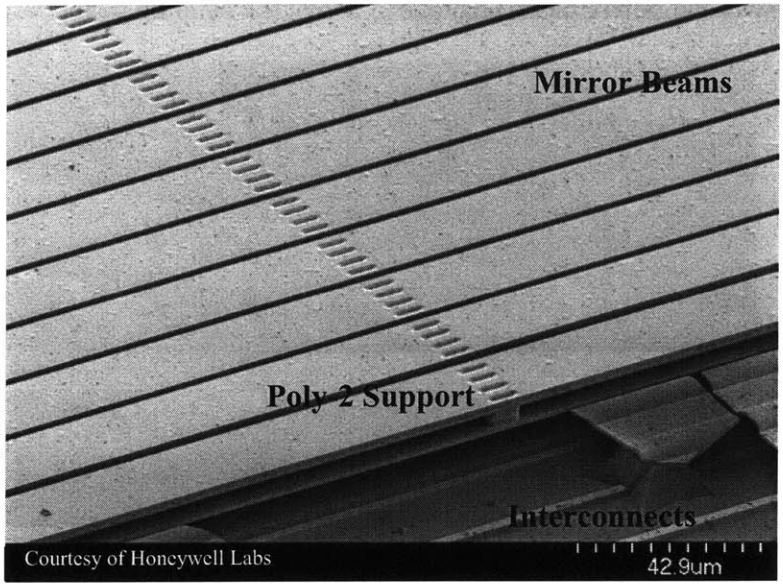

Figure 3.30: SEM of MEMS grating showing the double beam design, including the electrode, support structure, lower bending beam, and upper mirror beam.

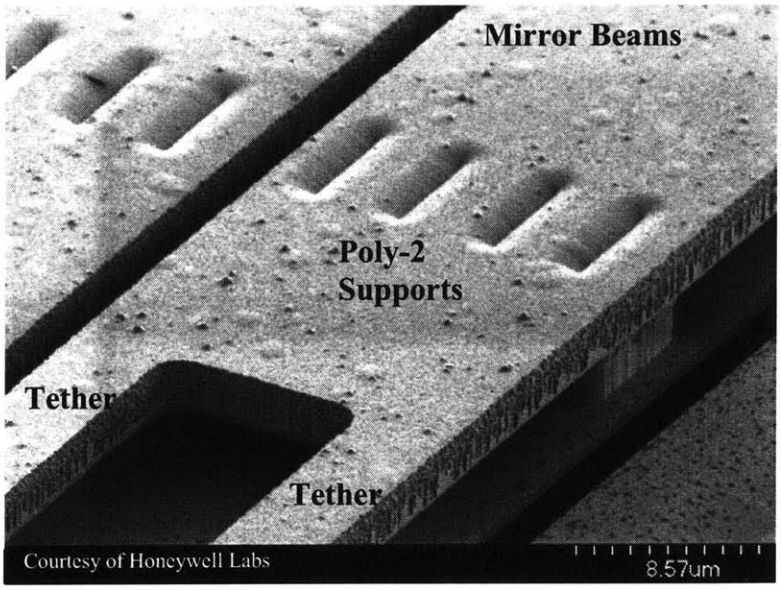

Figure 3.31: SEM showing detail of the mirror beam supports and the tethers

Figure 3.32 shows the underlying structure beneath the mirror beams and bending beams which have been removed. The electrodes and poly-1 post structure is evident, as well as the topography in the mirror layer (as a result of the poly-1 support). Figure 3.33 is a close-up of the entire three-layer polysilicon stack at the poly-1 support post. The definition of the electrode and the poly-0 pad is shown with a 2 micron space between them. The poly-1 beam, the conformal fill of the support post, and its connection to the pad is shown with the mirror beam unattached above the bending beam.

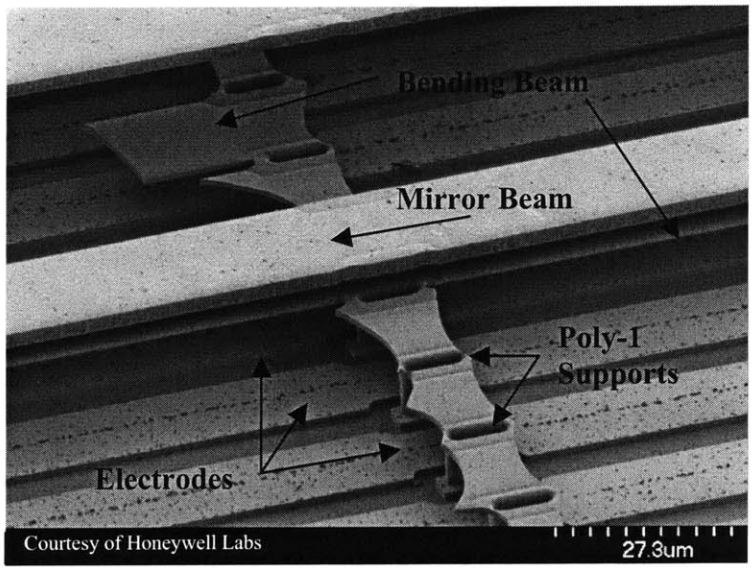

Figure 3.32: SEM showing two beam structure and supports with several beams removed to show the underlying support structure.

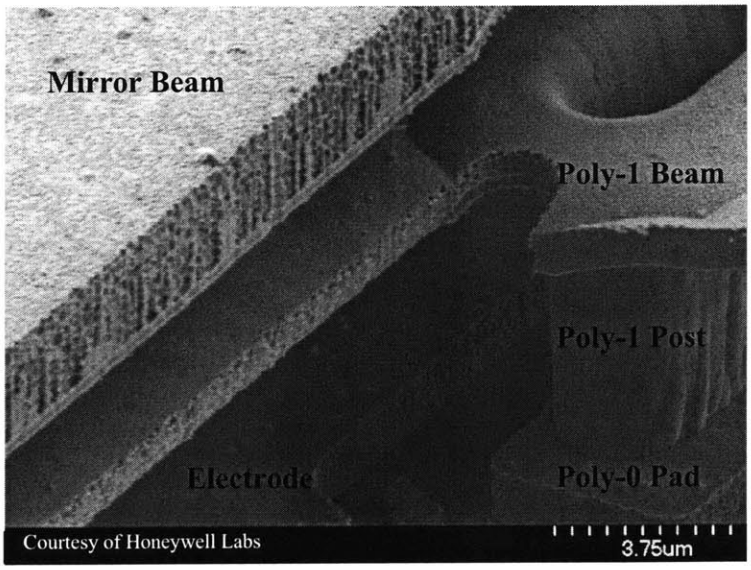

Figure 3.33: SEM showing all polysilicon layers and the detail of the lower support.

3.4 Summary

Two fabrication sequences were presented in this chapter: the stacked support design that did not result in functional devices, and the lateral support redesign that yielded functional Polychromator die. Process development required for thick sacrificial oxide layers, stress control, metalization, release, and packaging were discussed. Experimental results from devices fabricated using the lateral support process are presented in the following chapter.

Stress control and the deposition of thick oxide layers are the main fabrication challenges required prior to integrating the process into a manufacturing environment. The die-to-die and wafer-to-wafer repeatability of deposited film thickness, typical to that in semiconductor manufacturing (a few percent), is within acceptable limits for the device. The target film thicknesses should be chosen with these variations in mind. Base dielectric layers are insensitive to process variations, as long as they perform their function as insulators. The second sacrificial layer directly affects the maximum stable displacement of upper beam, and is the most critical thickness. Variations in lower gap and lower beam thickness affect the voltage-displacement characteristic of the device. The device should be designed such that maximum travel can be obtained insensitive to these variations. The upper beam thickness affects the MLNLS stiffness and is insensitive to process variations. Oxide etches can tolerate significant overetch into the underlying polysilicon layers and polysilicon etches can tolerate significant overetch into the underlying oxide layers. Designing the upper and lower gap to be more then required based on the variation in the process enables the device to function within specifications. The insensitivity to process variations, and the absence of a critical deposition thickness or etch depth makes the process robust and manufacturable.

Chapter 4: Experimental Results

This chapter describes the displacement characteristics of the fabricated devices. The electromechanical testing method used to measure vertical displacement is presented. The experimental results obtained using this method are then presented for grating designs of varying beam segment length. Comparison of these results to FDM simulations for multiple beam lengths enables extraction of the residual polysilicon stress. This value of stress is then used to compare the full voltage-displacement curve to the full MEMCAD model. The device performance as measured by an automated beam displacement measurement system, is then presented. Performing a short series of measurements on one element tests the repeatability of the measurement. Measuring the actuation characteristic over the span of many actuation cycles tests beam reliability. Measuring the voltage-displacement characteristic for each beam on the device tests the uniformity. Yield is reported as the number of working grating elements for each of several devices. Of the nonfunctional elements, the possible failure mechanisms are discussed.

4.1 Final Device Specifications

The devices reported in this chapter were built using the lateral support process with post-release gold metalization of the mirror beams. The thickness of the lower sacrificial gap was between 7.8 and 8 microns, depending on the wafer and the location of the die on the wafer. The bending beam thickness was measured to be 1.02 microns. The second sacrificial gap was between 3.8 and 3.9 microns depending on the wafer, as measured by the point of touchdown of the MLNLS. The mirror beam thickness was measured to be 2.55 microns. Comparisons to simulation in this chapter assume a lower gap of 8 microns, a lower polysilicon beam thickness of 1 micron, an upper gap of 3.8 microns, and an upper beam thickness of 2.5 microns.

4.2 Electromechanical Testing

To evaluate fabricated unpackaged devices, interference microscopy [41,42] is used to measure vertical movement of individual beam elements. To detect and quantify the vertical motion of two neighboring beams that are parallel and planar, an interference objective is used (Mirau-type double-beam, Nikon CF Plan EPI DI 10X). If the sample is tilted, parallel fringes will be produced on the device; these fringes result from the difference in height of the sample with respect to the microscope objective (Figure 4.1). The vertical displacement that corresponds to one fringe shift is half the incident wavelength. The wavelength of light used is 546 nanometers when using a narrow band optical filter; thus, the half fringe shift of the highlighted beam in Figure 4.1 represents 137 nanometers of vertical displacement. Using this technique, the deflection of each

beam can be measured as a function of applied voltage. This system is used for all unpackaged device testing, as described in Section 4.5.1.

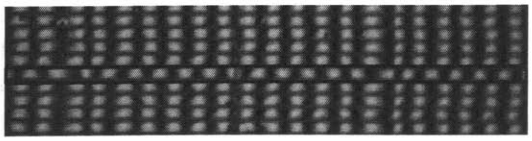

Figure 4.1: Grating elements are horizontal and the sample is tilted such that the axis of rotation is perpindicular to the beam elements and the fringes are produced perpindicular to the beam elements.

To test the packaged devices while maintaining cleanliness of the device, it is necessary to test the device through a calcium fluoride window. It was not possible to obtain fringes using the previously described interferometer through the window, so a Michelson microscope objective that provided access to the reference arm of the interferometer was used. A calcium fluoride window with the same thickness as the device window was inserted into the reference arm of the objective, and the position of the reference mirror was moved to match the focus of the sample arm. This matched the optical path length of the reference and sample arms of the interferometer, and enabled the fringes to be observed with a narrow band light-emitting diode light source. The wavelength of light used is 525 nanometers; thus, the seven fringe shifts of the highlighted beam in Figure 4.2 represent 1.84 microns of vertical displacement. The Michelson interferometer system (Michelson type double-beam, Nikon CF Plan EPI TI 5X) differs from the Mirau interferometer system in that the fringes do not cover the entire field of view, but are multiplied by an envelope function that limits the number of visible fringes. This system is used for automating testing.

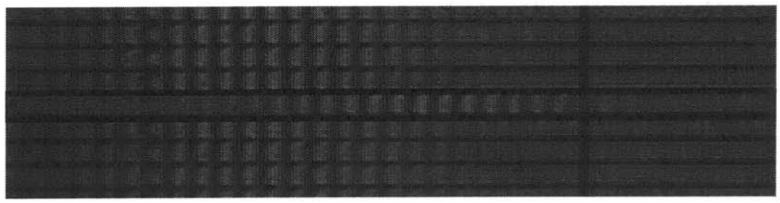

Figure 4.2: Fringe shift of actuated beam using Michelson interference microscopy.

4.3 Actuation Results

The measured voltage-displacement transfer functions, for devices with varying beam segment lengths, are shown in Figure 4.3. The die are from different wafers and the stress on each wafer is different, but the overall trends discussed in Section 2.2.2 and shown in Figure 2.11 can be observed in Figure 4.3. As the length of the beam segments is increased, the voltage necessary to actuate the grating elements decreases, and the displacement at the pull-in voltage is reduced. The devices reach between 3.5 and 3.9 microns of actuation between 40 and 125 volts. The grating elements with longer beam segments do not travel far enough, before becoming unstable, to exhibit the pull-in

protection feature of the design. These grating elements snap down and are stiffened enough by the MLNLS effect to stop them from contacting the underlying electrode and catastrophic failure. The grating elements with shorter beam segments make contact before becoming unstable. The plot shows the expected voltage-displacement characteristic after contact, at 3.8 microns; the two-beam structure becomes stiffer and more voltage is required to displace further. The upper mirror beam element is bent during this section of actuation.

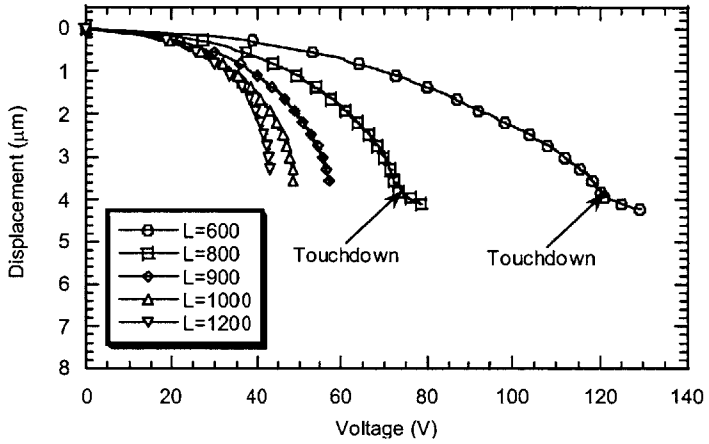

Figure 4.3: Measured voltage-displacement characteristic for various die with different grating element lengths from different wafers.

4.4 Comparison to Models

In order to validate the design methodology and the fabrication, the device actuation results are compared to simulations. The voltage-displacement curves are compared to FDM simulations to estimate the residual stress in the devices. Given this value for the residual stress, the structures are simulated in MEMCAD and then compared to the actuation characteristics before and after contact for the full MLNLS characteristics.

4.4.1 Stress Determination Using FDM

Stress is the only unknown parameter in the design. It is possible to estimate the stress by comparing simulation results to measured data for varying beam segment lengths. Simulations of two beam element lengths, 600 and 800, and the same process parameters are performed for varying stress. These simulations are then compared to experimental voltage-deflection data for the two chosen beam lengths from the same wafer (Figure 4.4 and Figure 4.5). Both sets of experimental data are close to matching the simulations of 15 MPa of tensile residual stress.

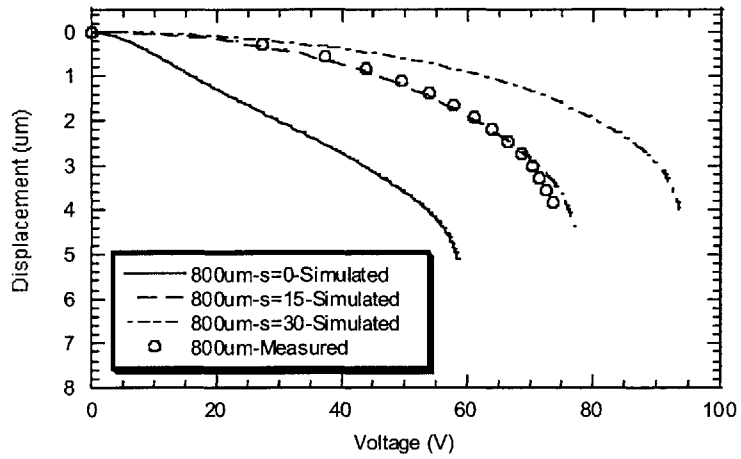

Figure 4.4: Displacement vs. voltage for varying residual beam stress simulated with an ideal structure, and measured on the 800 micron grating element.

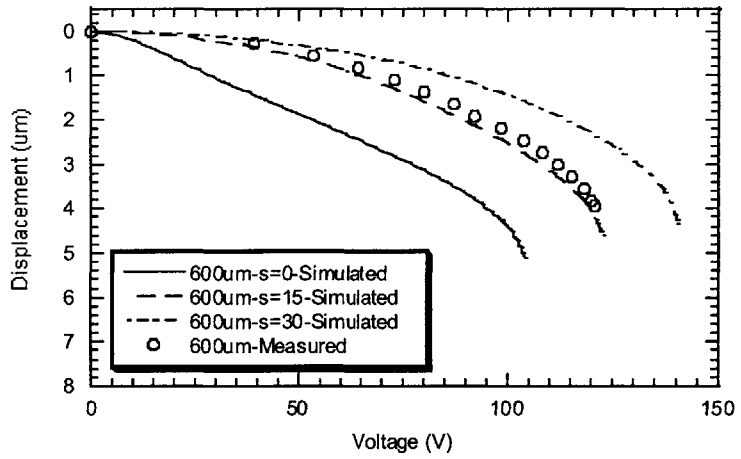

Figure 4.5: Displacement vs. voltage for varying residual beam stress simulated with an ideal structure, and measured on the 600 micron grating element.

4.4.2 MLNLS Characteristic Using MEMCAD

The simulated voltage-displacement characteristics, including actuation before and after contact, are compared to experiment (Figure 4.6). The experimental results showing features of the MLNLS concept agree extremely well with the simulated characteristics using 15 MPa of tensile residual stress. This validates the models used to design the structures, and the estimation of stress in the structure.

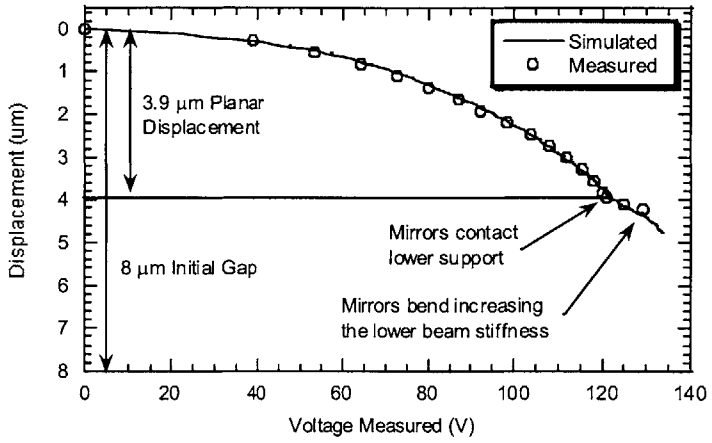

Figure 4.6: Plot of displacement versus voltage for the multi-layer nonlinear spring design. Data was obtained from coupled electromechanical MEMCAD simulations and from measurements of fabricated structures.

4.5 Device Performance

The grating element designs function very similarly to simulations of their actuation behavior. This section examines grating element performance over time and the functionality of all elements on a device. Tests with long duration are designed to observe if there is any drift or degradation of the voltage-deflection characteristic after multiple tests (repeatability) or after a longer period of repeated actuation (reliability). Tests of all elements on a device focus on the change in actuation characteristic across the device (uniformity) and how many of the beams function to a given specification (yield).

4.5.1 Automated Testing

To take large amounts of data from a large number of elements, an automated testing system was developed by Bardhan [42]. The system uses a limited search correlation function with up-sampled video-image data to compute the *spatial delay* between the fringe patterns on test and reference beams. This spatial delay is then converted into vertical displacement using the fact that the distance between fringes corresponds to half the wavelength of illuminating light. The measurement system is capable of resolving 1.1 nanometers minimum displacement, and was tested against calibration standards [50] and found to have an absolute error of 6.2 nanometers [42]. For more detailed analysis of the data, a 6^{th} order polynomial is fit to the data in the operating region. Data measured using this system agrees very well with simulation results (Figure 4.7).

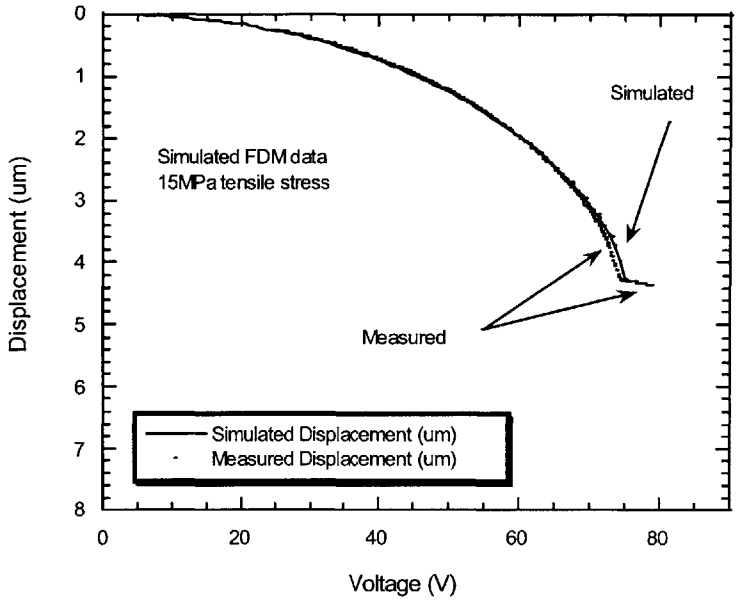

Figure 4.7: Measured data with the automated system and simulation.

4.5.2 Repeatability

To assess the repeatability of the automated measurement system, the complete voltage-displacement characteristic for one grating element is measured 64 times consecutively (Figure 4.8). The average voltage required for 3.5 microns of displacement is 72.1 volts with a standard deviation of 0.07 volts. There is no systematic variation with test number over the 9-hour measurement cycle indicating that there was negligible charge buildup or drift in the device. This result also demonstrates the robustness of the measurement procedure.

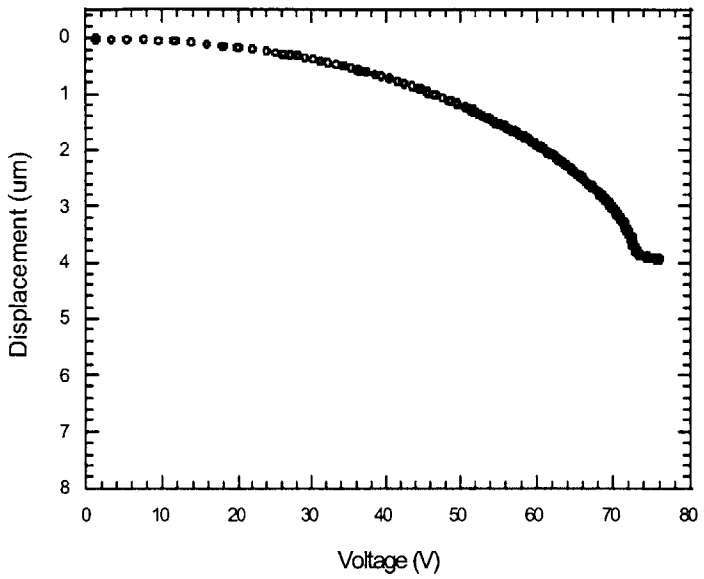

Figure 4.8: Displacement vs. voltage for 64 consecutive tests of one grating element.

4.5.3 Reliability

To test the reliability of the device over time, a 70-volt, 100-millisecond-period square wave was applied to one grating element. The voltage-displacement transfer function was measured 50 times, every 2500 cycles for a total of 10 hours. The variation in measurements was consistent with the repeatability of the measurement system. No systematic variation in transfer characteristic was observed after 125,000 cycles.

4.5.4 Uniformity

The uniformity of the device describes the variation in actuation characteristics over the 512 beams on the device. Voltage-displacement data is taken for each grating element on the device; the data are plotted as voltage, for a given set of displacements, vs. grating element number (Figure 4.9). The automated testing system acquired in excess of 60,000 data points over 8 days. The global average voltage required for 3.5 microns of displacement was 68.7 Volts, with a standard deviation of 0.85 Volts. After removal of a parabolic systematic variation of required voltage as a function of beam number across the device, the standard deviation was reduced to 0.55 Volts.

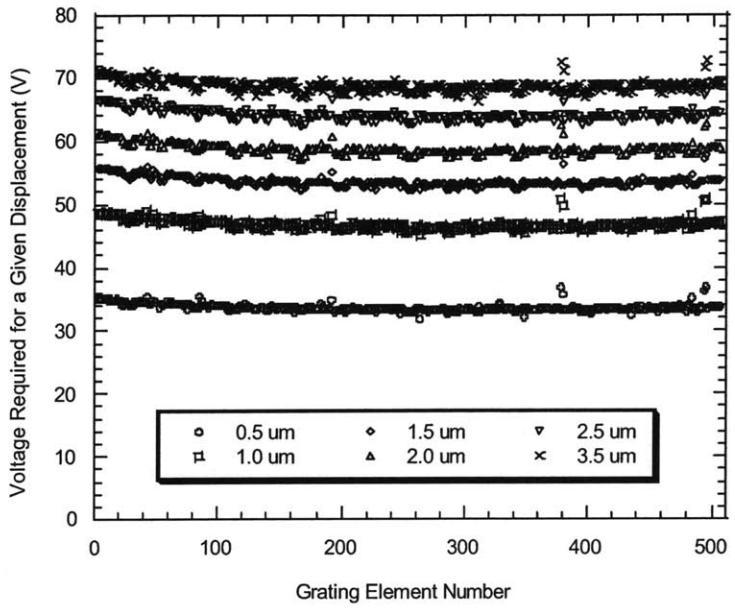

Figure 4.9: Voltage required for a given displacement for each grating element.

One possible contributing factor is a variation in polysilicon stress across grating elements. Another possible source for the variation in displacement characteristics is a non-uniform film thickness of oxide or poly across the one-centimeter wide array of grating elements. The 8-micron sacrificial oxide is known to have a four to five percent variation in film thickness from center to edge of the wafer. This variation corresponds to an approximately two percent variation across the die, which is a height difference of 0.16 microns. FDM simulations of this difference in lower gap thickness produce a 3-volt difference in actuation voltage at 3.5 microns displacement, which corresponds to the measured difference in actuation voltage. A parabolic variation in oxide thickness would produce the systematic variation observed in Figure 4.9.

4.5.5 Yield

The device yield is reported as a percentage of working beams. The yield of four fully packaged and tested devices is listed in Table 4.1. Yield ranged from 70% to 96% for these devices.

The devices exhibited several failure modes. Failures can occur at four main locations: the die, the wire bonds, the circuit board, and the drive electronics. On the die there are three observed problems; an adjacent beam is either mechanically or electrically connected to a beam under actuation in the grating area, or a beam two beams away from the beam under actuation is electrically connected to the actuated beam in the interconnects around the grating area (since the electrical interconnects are interleaved so that adjacent beams are electrically connected on opposite sides of the die). When there is an electrical short, the voltage measured by the voltage source monitoring voltmeter is half of the desired applied voltage, since the connected beam acts as a voltage divider.

When a wire bond has failed between the die and the interposer, or between the interposer and the circuit board, the voltage measured is the same as the voltage applied, but the beam does not move. If there is a short on the circuit board then two or more beams could actuate when they are not necessarily right next to each other. The entire package requires approximately 1600 solder or wirebond connections, for the 512 grating elements and 8 grounds.

Device #	Beam Length (um)	Electrode Length (um)	Maximum Voltage (V)	Maximum Displacement	Yield
2A9	900	16	72	3.8 um	90%
4A2	600	16	127	3.8 um	72%
4A6	800	16	78	3.8 um	70%
4A5	800	20	73	3.8 um	94%
4A2	600	16	130	3.8 um	96%

Table 4.1: Yield of packaged Polychromator devices.

The first packaged device tested had 90% yield. Failures for this device were attributed to random electrical and mechanical defects. The second and third packaged device had significantly lower yield. Failures for these devices occurred primarily in groups, where a beam two beams away from the beam under actuation would move. This was caused by misalignment in wirebonding. After re-wirebonding the circuit boards, the devices exhibited 94% for a new packaged device and 96% for a reworked package of a previously tested device. The remaining defects were equally attributed to a beam two beams away being shorted to the beam under actuation, poor wirebonds, and random defects. Significant improvement in packaging would enable the yield to increase to about 98% with the remaining 2% of nonfunctional elements caused by defects from particles or thin-film defects occurring during processing.

Chapter 5: Discussion and Conclusions

This chapter describes overall design limitations, uses of the technology developed, future work, and concludes with a summary of the work presented in this thesis. The scalability and limitations of the overall design and operation are discussed. Applications for the programmable diffraction grating and other applications for large planar travel are presented. Future work on the functionality, design, and fabrication of the Polychromator are addressed. The final section of the chapter draws conclusions from the design, simulation, fabrication, and testing of the Polychromator diffraction grating.

5.1 Scalability

The two-tiered structure was simulated with a 6 to 12 micron lower gap, which allows devices to achieve 3 to 6 microns of travel. The experimental results for a device with an 8-micron lower gap validated the simulations. Fabricated devices within the range simulated in this thesis should be consistent with the simulations. The two-tiered MLNLS design will function for lower travel than originally designed; however, if the sacrificial gap were to be reduced to a similar thickness to the beam thickness, the motion of the beam would be reduced to one-third of the gap instead of half the gap, since the beam would no longer be in the stress stiffened region of operation.

Several factors can be adjusted to increase the amount of achievable actuation. The actuation voltage increases for increasing gap, and decreases for increasing beam length. If beam segments are made too long, they may difficult to reliably fabricate and they may not be robust in operation. As gaps are increased electrical cross talk between elements will increase. The most significant challenge involved in scaling the design out of the current range is in fabrication. The current fabrication process would not scale well out of the current range of lower gaps, due to the difficulty depositing and etching thick oxide layers. If a different film was deposited instead of oxide, was compatible with polysilicon processing, and could be sacrificially etched, the process change would alleviate this constraint on scalability.

5.2 Applications

The Polychromator was designed for use in a remote chemical sensing system. The diffraction grating acts as an optical processor that correlates the spectral features of an unknown sample with the known spectral features of a known reference species in the mid-infrared. The two spectra are compared and a simple detector can be used to determine the presence of a specific chemical. The device can be used for other applications of a diffraction grating, or the planar vertical motion could be used for a completely different application.

The diffraction grating could be used as an optical filter, since it can be programmed to diffract light in a narrow wavelength band. By programming the grating to diffract light in a narrow wavelength band, and scanning this peak through a range of wavelengths, the filter can be used as a spectrometer to record the intensity of light over the wavelength range in the mid-infrared. The diffraction grating could also be used as an optical switch for infrared light. In the reflective state light could be collected and in the diffractive state light could be blocked, or visa versa. This switching concept is similar to an optical switch using diffraction at visible wavelengths for display applications [2].

5.3 Future Work

The current fabricated device achieves approximately four microns of displacement. The next step towards the initial goal of 6 microns of planar vertical motion is the fabrication of devices with 12-micron sacrificial oxide layers. Once the current devices are incorporated into optical correlation spectrometer systems and are tested, additional functionality from the device may be necessary. For future Polychromator devices, it may be desirable to design the device to fit into an existing manufacturing process. The current design requires a custom fabrication process, so for production the process would have to be integrated into a manufacturing environment.

Increasing the yield of the device will require the elimination of the main sources of failure, which occur during packaging, making electrical connections, or are defects in fabrication. Fabrication of the devices in a production environment in an integrated circuit facility would greatly reduce the defects. Packaging the device and connecting the 512 elements to drive voltages directly would involve significant development but could significantly increase yield. One method is to integrate drive electronics on chip, though this would significantly complicate fabrication. Another method is to attach the die directly to another electronics chip through electrical connections using flip chip bonding or through wafer vias and solder bonding technology.

5.4 Conclusions

This thesis describes the design, simulation, fabrication, and testing of a large vertical displacement planar actuator and an application – the mid-infrared Polychromator. Particular attention to the coupling between design and fabrication was essential to producing a functional device.

The mid-infrared Polychromator uses a similar structural design and fabrication sequence to the previously built near-infrared Polychromator. The near-infrared design is described as background for the design presented in this thesis. The specifications for the mid-infrared design – 6 microns planar travel of approximately 500 elements, each 20 microns wide and one centimeter long – dictate a new, highly constrained, actuator design. The design uses thick gaps and stress stiffening of the actuated beam to achieve large travel, and a multi-layer nonlinear spring effect, created by contact between the

upper beam and the lower beam, to stiffen the structure and prevent pull-in and device failure.

The functionality of the device was investigated using a hierarchical simulation strategy. First, the design is simulated using energy methods, which provide rapid insight into the design space by approximating the device performance with an analytical model. Second, finite difference methods are used to more accurately model the voltage-displacement transfer function of the lower actuated beam. Third, MEMCAD simulations are used to predict the behavior of the multi-layer nonlinear spring design through its full range of operation.

Careful attention was given to end effects and support structure. Deleterious end effects, as a result of stress relaxation and resulting compression in the centimeter long mirror elements, were eliminated by rigidly supporting the end of the elements, which prevented them from compressing. Stiff supports were realized by maximizing stress transfer from one side of the support to the other, and lateral posts enabled an electrode to travel beneath the support without the need for a critical dielectric.

Two different processes were developed. The fabrication of the stacked support structure failed due to processing limitations. The lateral support structure was a significant process and design simplification. Fabrication of the lateral support structure resulted in functional devices. Significant challenges were addressed in process development, including the development of a thick oxide layer deposition process, stress control, metalization, release, and packaging. The resulting fabrication process is insensitive to process variations, making it robust to a manufacturing environment.

Fabricated devices were tested and the results agreed extremely well with simulation and operation specifications. The residual stress in the polysilicon, which is the only unknown parameter of the fabricated device, is extracted consistently between different devices on the same wafer. This was found by comparing simulated voltage-displacement curves with experimental results. Automated testing of the voltage-displacement transfer function enabled investigation of the repeatability, reliability, and uniformity of the device. The repeatability over 64 consecutive tests of the actuation characteristic using the automated measured system showed no systematic variation and had a standard deviation of 0.07 Volts at maximum displacement. A grating element was tested for reliability and operated for 125,000 cycles without failure or noticeable degradation. The voltage displacement characteristic across the device had a systematic variation, which might be caused by film thickness variations. The standard deviation of the voltage across the entire device required for maximum displacement was 0.5 Volts once the systematic variation was removed. The final yield for the packaged and tested devices was between 90 and 96 percent.

Appendix A: Mask Specifications

A.1 Mask Layout

Devices with a range of lower gap thicknesses from 6 to 12 microns were designed. In order to have operating devices at each of these gaps with one mask set, beam lengths on the mask set were chosen to span the design space. Simulations of device behavior (Chapter 2) were used to choose these designs. The wafer size permits placement of 12 Polychromator die per wafer and 4 smaller die with test structures (Figure A.1). Design parameters for the 12 designs are shown in Table A.1. Beam lengths, as illustrated in Figure A.2, range from 600 to 1200 microns, and various electrode width and ground spacer configurations, are shown in Figure A.3. The lower gap at which an 80V or 150V driver would be able to operate the device is listed in Table A.1. Comments describe the expected functionality of the various designs. The designs are located on the wafer such that the devices with the highest expectation for success are located in the center of the wafer, since the center has the most uniform and defect free processing. The remaining designs are located around the center four.

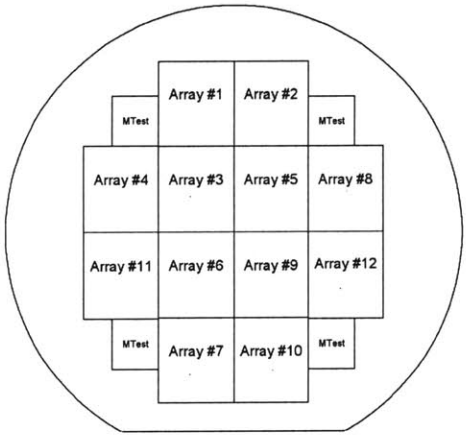

Figure A.1: Four inch wafer layout for polychromator.

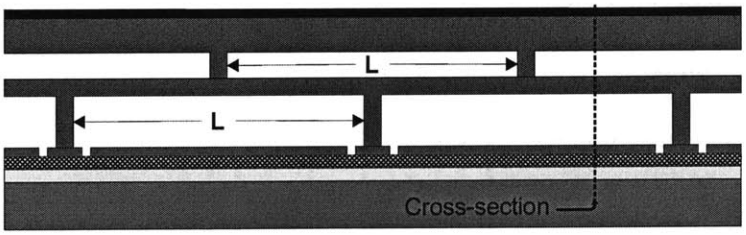

Figure A.2: Side view of structure with definition of beam length 'L'.

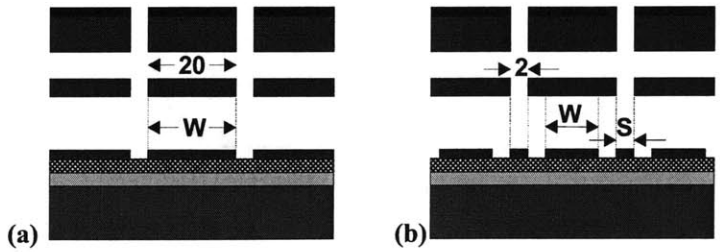

Figure A.3: Beam end on view of (a) electrode width 'W' or (b) decreased electrode width 'W' with or without a grounded spacer 'S'.

Die ID #	Beam Length μm	Electrode Width μm	Ground Spacer	Gap 80 V	Gap 150 V	Comments
1	600	20	No	6	6-8	Simple DSB structure
2	600	16	Yes	6	6-8	Reduce cross-talk
3	700	20	No	6-7	6-10	Operate at 10um gap under 150V
4	700	16	No	6-7	6-10	Operate at 10um gap under 150V
5	800	20	No	6-8	6-11	Simple DSB structure
6	800	16	Yes	6-7	6-11	Reduce cross-talk
7	800	14	No	6-7	6-10	Minimize electrical cross-talk
8	900	20	No	6-9	6-12	Operate at 12um gap under 150V
9	900	16	No	6-9	6-12	Operate at 12um gap under 150V
10	1000	20	No	6-10	6-12	Simple DSB structure
11	1000	16	Yes	6-9	6-12	Reduce cross-talk
12	1200	16	No	6-10	6-12	Operate at 12um under 80V

Table A.1: Grating array designs and specifications.

A.2 Mask Layer Descriptions

The stacked support design requires 10 masks for fabrication (Table A.2), and the lateral support design requires 7 masks for fabrication (Table A.3). For the stacked support process, mask layers 2, 5, and 8 are used to define the polysilicon; mask layers 4 and 6 are used to define holes, or *vias*, in the oxide layers to anchor the subsequent polysilicon layers. Mask layer 1 is used to define a recess in the silicon wafer to offset the isolation pad created by mask layer 3; it also minimizes topography. Mask layer 7 is used to define anti-stiction dimples between the two active polysilicon layers. Mask layers 9 and 10 are used to define the bond pads and the reflective mirror layer. For the lateral support process, mask layers 1, 3, and 5 are used to define the polysilicon. Mask layers 2 and 4 define vias in the oxide, and mask layers 6 and 7 define the bond pads and mirror surface.

Layer	Mask Type	Description	Aligned to
1	Dark Field	Recess for SiN pads	silicon wafer
2	Light Field	Poly 1	Layer 1
3	Light Field	SiN pads beneath P1P2vias	Layer 2
4	Dark Field	P1P2vias	Layer 2
5	Light Field	Poly 2	Layer 4
6	Dark Field	P2P3vias	Layer 5
7	Dark Field	Dimples beneath Poly 3	Layer 5
8	Light Field	Poly 3	Layer 7
9	Light Field	Bond Pad Vias	Layer 8
10	Light Field	Mirror Metal	Layer 8

Table A.2: Mask Descriptions for Stacked Support Process.

Layer	Mask Type	Description	Aligned to
1	Light Field	Poly 0	silicon wafer
2	Dark Field	P1P2vias	Layer 1
3	Light Field	Poly 2	Layer 2
4	Dark Field	P2P3vias	Layer 3
5	Light Field	Poly 3	Layer 3
6	Light Field	Bond Pad Vias	Layer 5
7	Light Field	Mirror Metal	Layer 5

Table A.3: Mask Descriptions for Lateral Support Process.

Appendix B: Detailed Process Flows

B.1 Stacked Support Process Flow

1. Starting Wafers
2. Silicon Recess Etch 1.5μm
3. Frontside Electrical Passivation
4. Deposit LPCVD Nitride 7000Å
5. Deposit and Blanket Implant Poly 1
6. Pattern and Etch Poly 1
7. Deposit LPCVD Nitride 1μm
8. Deposit Aluminum Etch Stop
9. Nitride Isolation Pad Photo and Etch
10. Backside Film Strip 1μm Nitride
11. Deposit LTO-1 12μm
12. Pattern and Etch LTO1 (Poly 2 –Poly 1 Posts)
13. Deposit and Blanket Implant Poly2
14. Pattern Poly 2
15. Deposit LTO2 7μm
16. Pattern and Etch LTO2 (Dimples)
17. Pattern and Etch LTO2 (Poly 3 – Poly 2 Posts)
18. Deposit Poly 3 and Blanket Implant
19. Photo and Etch Poly 3
20. Anneal All Poly Layers
21. Backside Film Strip Poly 3 / 7 μm Oxide / Poly 2
22. Pattern for Bond Pad Metal
23. Deposit Pad Metal and Liftoff
24. Pattern for Mirror Metal
25. Deposit Mirror Metal and Liftoff
26. Die Sawing of Wafers
27. Etch Sacrificial Layers (Die Level)

B.2 Lateral Support Process Flow

1. Starting Wafers
2. Frontside Electrical Passivation
3. Deposit LPCVD Nitride 4000Å
4. Deposit and Blanket Implant Poly 1
5. Pattern and Etch Poly 1
6. Deposit Gap Oxide 1
7. Pattern and Etch Gap Oxide 1 (Poly 2 –Poly 1 Posts)
8. Ground Pad Corner Rounding Backup Plan
9. Deposit and Blanket Implant Poly2
10. Pattern Poly 2
11. Deposit Gap Oxide 2
12. Pattern and Etch LTO2 (Poly 3 – Poly 2 Posts)
13. Deposit Poly 3 and Blanket Implant
14. Photo and Etch Poly 3
15. Anneal All Poly Layers
16. Backside Film Strip Gap Oxide 2/ Poly 2
17. Pattern for Bond Pad Metal
18. Deposit Pad Metal and Liftoff
19. Die Sawing of Wafers
20. Etch Sacrificial Layers (Die Level)
21. Deposit Mirror Metal

References

[1] L. J. Hornbeck, "Current status of the digital micromirror device (DMD) for projection television applications" *Technical Digest, Electron Devices Meeting*, pp. 381–384, 1993.

[2] O. Solagaard, F. S. A. Sandejas, and D. M. Bloom, "Deformable Grating Optical Modulator," *Optics Letters*, vol. 17, pp. 688-690, 1992.

[3] M.B. Sinclair, M.A. Butler, A.J. Ricco, and S.D. Senturia,"Synthetic Spectra: A Tool for Correlation Spectroscopy," *Applied Optics 36*, pp. 3342-3348 (May 20, 1997)

[4] M.B. Sinclair, M.A. Butler, S.H. Kravitz, W.J. Zubrzycki, and A.J. Ricco, "Synthetic Infrared Spectra," *Optics Letters 22*, pp.1036-1038 (July 1, 1997)

[5] G.B. Hocker, D. Youngner, E. Deutsch, A. Volpicelli, S. Senturia, M. Butler, M. Sinclair, T. Plowman, and A. J. Ricco, "The Polychromator: A Programmable MEMS Diffraction Grating for Synthetic Spectra," *Solid-State Sensor and Actuator Workshop,* Hilton Head Island South Carolina, pp. 89-91, June 2000.

[6] H. Fujita, "A Decade of MEMS and its Future," *IEEE Workshop on Micro Electro Mechanical Systems, (MEMS '97)*, pp. 1-7, 1997

[7] P. F. Van Kessel, L. J. Hornbeck, R. E. Meier, M. R. Douglass, "A MEMS-Based Projection Display" *Proceedings of the IEEE*, vol. 86, no. 8, pp. 1687-1704, August 1998.

[8] K. Sato, M. Shikida, "Electrostatic Film Actuator with a Large Vertical Displacement," *Micro Electro Mechanical Systems, (MEMS '92)*, Travemünde Germany, pp. 1-5, February 4-7, 1992.

[9] A. Tuantranont, V. M. Bright, "Segmented Silicon-Micromachined microelectromechanical Deformable Mirrors for Adaptive Optics," *IEEE Journal on Selected Topics in Quantum Electronics*, Vol. 8, No. 1, 2002.

[10] T. Bifano, R. K. Mali, J. Perreault, M. Horenstein, D. Koester, "MEMS Deformable Mirrors for Adaptive Optics," *Solid-State Sensor and Actuator Workshop,* Hilton Head Island South Carolina, pp. 71-74, June 1998.

[11] M. Huja, M. Husak, "Thermal microactuators for optical purpose," *International Conference on Information Technology: Coding and Computing*, pp. 137-142, 2001.

[12] J. W. Judy, T. Tamagawa, D. L.Polla, "Surface micromachined linear thermal microactuator," *International Electron Devices Meeting*, pp. 629-632, 1990.

[13] M. Ataka, A. Omodaka, N. Takeshima, H. Fujita, "Fabrication and operation of polyimide bimorph actuators for a ciliary motion system," *Journal of Microelectromechanical Systems*, Vol. 2. pp. 146 –150, 1993.

[14] M. Pozzi, T. King, "Piezoelectric actuators in micropositioning," *Journal of Engineering Science and Education*, Vol. 10, pp. 31-3 Feb 2001 6

[15] H. Toshiyoshi, D. Kobayashi, H. Fujita, T. Ueda, "A Piezoelectric Psuedo-static Actuator for Large Displacement under AC voltage operation," *International Conference on Solid State Sensors and Actuators, 1995. (TRANSDUCERS '95)*, Stockholm Sweden, pp. 389-392, 1997.

[16] T. Kawabata, M. Ikeda, H. Goto, M. Matsumoto, T. Yada, "The 2-Dimensional Micro Scanner Integrated with PZT Thin Film Actuator," *International Conference on Solid State Sensors and Actuators, (TRANSDUCERS '97)* Chicago USA, Vol.1, pp. 339-342, 1997.

[17] H. Toshiyoshi, D. Miyauchi, H. Fujita, "Micromechanical fiber optic switches based on electromagnetic torsion mirrors," *IEEE/LEOS Summer Topical Meetings* , pp. II/23 -II/24, 1998

[18] C. Liu, T. Tsao, Y.-C. Tai, C.-M. Ho, "Surface Micromachined Magnetic Actuators," *IEEE Workshop on Micro Electro Mechanical Systems, (MEMS '94)*, pp. 57-62, 1994.

[19] L. Houlet, P. Helin, T. Bourouina, G. Reyne, E. Dufour-Gergam, H. Fujita, "Movable vertical mirror arrays for optical microswitch matrixes and their electromagnetic actuation," *IEEE Journal on Selected Topics in Quantum Electronics*, Vol. 8, pp. 58-63, 2002.

[20] F. Kawai, P. Cusin, S. Konishi, "Thin flexible end-effector using pneumatic balloon actuator," *The Thirteenth Annual International Conference on Micro Electro Mechanical Systems, (MEMS 2000)*, pp. 391–396, 2000.

[21] X Yang, Y.-C. Tai, C.-M. Ho, "Micro bellow actuators," *International Conference on Solid State Sensors and Actuators, (TRANSDUCERS '97),* Chicago USA, Vol. 1, pp. 45-48, 1997.

[22] Y.-C. Su, L. Lin, A. P. Pisano, "Water-powered, osmotic microactuator," *The 14th IEEE International Conference on Micro Electro Mechanical Systems, (MEMS 2001)*, pp. 393-396, 2001.

[23] L. Shi-Sheng, E. Motamedi, M. C. Wu, "Surface-micromachined free-space fiber optic switches with integrated microactuators for optical fiber communication systems," *International Conference on Solid State Sensors and Actuators, (TRANSDUCERS '97)*, Chicago USA, Vol. 1, pp. 85-88, 1997.

[24] S. R. Bhalotra, J. D. Mansell, H. L. Kung, D. A. B. Miller, "Parallel-plate MEMS Mirror Design for Large On-resonance Displacement," *IEEE/LEOS International Conference on Optical MEMS*, pp. 93–94, 2000.

[25] T. Akiyama, D. Collard, H. Fujita, "Scratch drive actuator with mechanical links for self-assembly of three-dimensional MEMS," *Journal of Microelectromechanical Systems*, Vol. 6, pp. 10-17, 1997.

[26] R.Yeh, S.Hollar, K.S.J.Pister, "Single mask, large force, and large displacement electrostatic linear inchworm motors," *The 14th IEEE International Conference on Microelectromechanical Systems, (MEMS 2001),* pp. 260 –264, 2001.

[27] H. Chen, C. Chang, J. Chen, J. Chio, K. Yen, F. Xiao, P. Chang, "Fabrication of a Micromachined optical modulator using the CMOS process," *Transducers '99*, Sendai Japan, pp. 808-811, June 7-10 1999.

[28] A. H. Epstein, S. D. Senturia, G. Anathasuresh, A. Ayon, K. Breuer, K.-S. Chen, F. Ehrich, G. Gauba, R. Ghodssi, C. Groshenry, S. Jacobson, J. Lang,; C.-C. Mehra, J. Mur Miranda, S. Nagle, D. Orr, E. Piekos, M. Schmidt, G. Shirley, M. S. Spearing, C. S. Tan, Y-S. Tzeng, I. A. Waitz, "Power MEMS and microengines," *International Conference on Solid State Sensors and Actuators, (TRANSDUCERS '97) Chicago*, Vol. 2 , pp. 753 –756, 1997.

[29] L. Fan, M. C. Wu, K. D. Choquette, M. H. Crawford, "Self-assembled microactuated XYZ stages for optical scanning and alignment," *International Conference on Solid State Sensors and Actuators, 1997. (TRANSDUCERS '97)*, Chicago USA, Vol.1, pp. 319-322, 1997.

[30] L. Y. Lin, J. L. Shen, S. S. Lee, G. D. Su, M. C. Wu, "Microactuated micro-XYZ stages for free-space micro-optical bench," *Tenth Annual International Workshop on Microelectromechanical Systems,. (MEMS '97)*, pp. 43-48, 1997.

[31] R. A. Conant, P. M. Hagelin, U. Krishnamoorthy, O. Solgaard, K. Y. Lau, R. S. Muller, "A Raster-scanning Full-motion Video Display Using Polysilicon Micromachined Mirrors," *Transducers '99*, Sendai Japan, pp. 1456-1459, June 7-10 1999.

[32] J. R. Reid, V. M. Bright, J. H. Comtois, "Automated Assembly of Flip-Up Mirrors," *International Conference on Solid State Sensors and Actuators, (TRANSDUCERS '97)*, Chicago USA, vol.1, pp. 347-350, 1997.

[33] R. T. Chen, H. Nguyen, M. C. Wu, "A low voltage micromachined optical switch by stress-induced bending," *Twelfth IEEE International Conference on Microelectromechanical Systems, (MEMS '99)*, pp. 424 -428, 1999.

[34] J. E. Ford, V. A. Aksyuk, D. J. Bishop, J. A. Walker, "Wavelength add-drop switching using tilting micromirrors," *Journal of Lightwave Technology*, Vol. 17, pp. 904 –911, 1999.

[35] "The scanned grating light valve ^{TM} display: a technology update," *12th Annual Meeting IEEE Lasers and Electro-Optics Society (LEOS '99)*, Vol. 1, pp. 214 -215, 1999.

[36] E. S. Hung, *Positioning, Control, and Dynamics of Electrostatic Actuators for Use in Optical and RF Systems*, Ph.D. Thesis, Massachusetts Institute of Technology, 1998.

[37] B. Wagner, K. Reimer, A. Maciossek, U. Hofmann, "Infrared Micromirror Array with Large Pixel Size and Large Deflection Angle," *International Conference on Solid State Sensors and Actuators, (TRANSDUCERS '97)*, Chicago USA, Vol. 1, pp. 75-78, 1997.

[38] D. M. Burns, and V. M. Bright, "Nonlinear Flexures for Stable Deflection of an Electrostatically Actuated Micromirror," *Proc. SPIE: Microelectronics Structures and MEMS for Optical Processing III*, Vol. 3226, pp. 125-135, Sept. 1997.

[39] P. M. Osterberg, and S. D. Senturia, "M-TEST: A Test Chip for MEMS Material Property Measurement Using Electrostatically Actuated Test Structures," *Journal of Microelectromechanical Systems,* Vol. 6, No. 2, pp. 107-118, June 1997.

[40] E. S. Hung, S. D. Senturia, "Extending the Travel Range of Analog-Tuned Electrostatic Actuators," *Journal of Microelectromechanical Systems*, Vol. 8, pp. 497-505, 1999.

[41] A.M. Volpicelli, "Automation of Electrostatic Material Property Measurements Procedures," M. Eng. Thesis, MIT, February 2000.

[42] J. P. Bardhan, "Calibration of a Microvision System for MEMS Device Characterization" M. Eng. Thesis, MIT, June 2001.

[43] *Coventor*, Formerly *Microcosm Technologies*, www.coventor.com.

[44] M. Hopgood, "Control System Implementation for Grating-Element Positioning and Modulation of the Polychromator," M. Eng. Thesis, MIT, May 1998.

[45] S. D. Senturia, *Microsystem Design*, Kluwer Academic Publishers, Norwall, MA, 2001.

[46] R. Legtenberg, H. A. C. Tilmans, "Electrostatically Driven Vacuum-Encapsulated Polysilicon Resonators, Part I. Design and Fabrication," *Sensors and Actuators A*, vol. 45, pp. 57-66, 1994.

[47] U. Srinivasan, M. R. Houston, R. T. Howe, R. Maboudian, "Self-Assembled Fluorocarbon Films for Enhanced Stiction Reduction," *Transducers '97*, Chicago USA, pp. 1399-1402, June 16-19, 1997.

[48] *Novellus Systems Inc.*, 81 Vista Montana, San Jose, CA, 95134.

[49] R. Ghodssi, L. G. Frechette, S. F. Nagle, X. Zhang, A. A. Ayon, S. D. Senturia, M. A. Schmidt, "Thick Buried Oxide in Silicon (TBOS): An Integrated Fabrication Technology For Multi-Stack Wafer-Bonded MEMS Processes," *Transducers '99*, Sendai Japan, pp. 1456-1459, June 7-10 1999.

[50] E. R. Deutsch, "Development of Calibration Standards for Accurate Measurement of Geometry in Microelectromechanical Systems," M. S. Thesis, MIT, June 1998.

3521 - 1